ABSTRACT

Title of dissertation: Cryogenic Test of the Gravitational Inverse-Square Law Below 100-Micrometer Length Scales

Krishna Raj Yethadka Venkateswara, Doctor of Philosophy, 2010

Dissertation directed by: Professor Ho Jung Paik
Department of Physics

The inverse-square law is a hallmark of theories of gravity, impressively demonstrated from astronomical scales to sub-millimeter scales, yet we do not have a complete quantized theory of gravity applicable at the shortest distance scale. Problems within modern physics such as the hierarchy problem, the cosmological constant problem, and the strong *CP* problem in the Standard Model motivate a search for new physics. Theories such as large extra dimensions, 'fat gravitons,' and the axion, proposed to solve these problems, can result in a deviation from the gravitational inverse-square law below 100 μm and are thus testable in the laboratory.

We have conducted a sub-millimeter test of the inverse-square law at 4.2 K. To minimize Newtonian errors, the experiment employed a near-null source, a disk of large diameter-to-thickness ratio. Two test masses, also disk-shaped, were positioned on the two sides of the source mass at a nominal distance of 280 μm. As the source was driven sinusoidally, the response of the test masses was sensed through a superconducting differential accelerometer. Any deviations from the inverse-square

law would appear as a violation signal at the second harmonic of the source frequency, due to symmetry.

We improved the design of the experiment significantly over an earlier version, by separating the source mass suspension from the detector housing and making the detector a true differential accelerometer. We identified the residual gas pressure as an error source, and developed ways to overcome the problem. During the experiment we further identified the two dominant sources of error − magnetic cross-talk and electrostatic coupling. Using cross-talk cancellation and residual balance, these were reduced to the level of the limiting random noise.

No deviations from the inverse-square law were found within the experimental error (2σ) down to a length scale $\lambda = 100$ μm at the level of coupling constant $|\alpha| \leq 2$. Extra dimensions were searched down to a length scale of 78 μm ($|\alpha| \leq 4$). We have also proposed modifications to the current experimental design in the form of new tantalum source mass and installing additional accelerometers, to achieve an amplifier noise limited sensitivity.

Cryogenic Test of the Gravitational Inverse-Square Law Below 100-Micrometer Length Scales

by

Krishna Raj Yethadka Venkateswara

Dissertation submitted to the Faculty of the Graduate School of the
University of Maryland, College Park in partial fulfillment
of the requirements for the degree of
Doctor of Philosophy
2010

Advisory Committee:
Professor Ho Jung Paik, Chair/Advisor
Professor Theodore Allan Jacobson
Professor M. Coleman Miller
Dr. M. Vol Moody
Professor Peter S. Shawhan

Dedication

To my parents.

Acknowledgments

Over the course of this thesis and my graduate studies I have been most fortunate to have interacted with and received guidance from a number of people. They have not only made this thesis possible, but have influenced my outlook and motivation towards experimental physics.

First and foremost, I'd like to thank my advisor Professor Ho Jung Paik for giving me an invaluable opportunity to work on challenging and extremely interesting projects over the past six years. Throughout my graduate studies, he has kept me focused and motivated. I have always admired and have been influenced by his persistence, and his insistence in understanding the underlying physics in every problem. His optimistic attitude and excellent guidance have been instrumental in making this daunting experiment possible.

I am also very grateful to Dr. M. Vol Moody, who has been an excellent mentor to me in the laboratory. His thorough and deep insight, and problem solving skills, not to mention his great sense of humor, have always inspired me. I often turned to him when I was stuck, and inevitably, discussions with him helped illuminate the problem and the solution. He also provided major assistance with the data analysis tools.

I'm very grateful to Dr. Violeta A. Prieto. To me, she set the standard for performing excellent graduate research work. Her work-ethic and determination were very inspiring. She laid the foundation for this experiment and assisted greatly in improving it.

Ron Norton's technical help with software and hardware are greatly appreciated, as are the lively discussions we've had on physics and other issues. I would like to thank Lvyuan Chen for performing source-metrology error calculations and general assistance with this experiment. I'm also very grateful to Dr. Peter Shawhan for discussions and some insightful suggestions for this experiment.

Russell Wood has been a fantastic teacher and friend, outside the lab. His immense technical expertise and knowledge in machining proved invaluable in building components for my projects. I'm very grateful for his assistance and his friendship.

I'm grateful to some of my closest friends Aswin Sankaranarayanan, Ashwin Swaminathan, Jagan Sankaranarayanan, Karthik Doddaballapur, Mahesh Ramachandran and Sunil Dorairajan for supporting me.

I owe my deepest thanks to my parents and my brother who have always been very supportive and have encouraged me to do well at my graduate studies.

This work has been supported by the National Science Foundation grants PHY-0244966 and PHY-0523320, and NASA grant NAG-32874.

Table of Contents

List of Tables

List of Figures

Chapter 1

Introduction and Review of Previous Inverse-Square Law Experiment

General Relativity (GR) has served as the best description of gravity for nearly a hundred years now. It has been tested very impressively over a wide range of distance scales, varying from the very large cosmological scales down to very short distances below 100 μm. Yet it has not been fully reconciled with the other great success of the twentieth century physics − the quantum mechanical description of the universe, including the Standard Model (SM). GR is non-renormalizable and a unified quantum theory of gravity, applicable at the highest energy or smallest length scale, does not yet exist. Since we have good reason to believe the quantum mechanical description at small length scales (electroweak scale), it is reasonable to hypothesize that GR breaks down at some length scale and the gravitational force deviates from the Newtonian inverse-square law (ISL).

It is thus very important to explore the gravitational interactions at small length scales. This experiment aims to test the ISL of gravity to better than one part in 10 on 100-μm distance scale and one part in one at 47-μm range. It is an improvement over Prieto's experiment [1], and employs very similar principles, devices and techniques. In this chapter, I will briefly review the theoretical motivations for the experiment and also the results and conclusions of [1].

Figure 1.1 shows the present limits on the coupling (α) and range (λ) of deviations in a generalized Yukawa potential of the form [2, 3, 4, 5]:

$$V(r) = -G\frac{m_1 m_2}{r^2}[1 + \alpha e^{-r/\lambda}]. \tag{1.1}$$

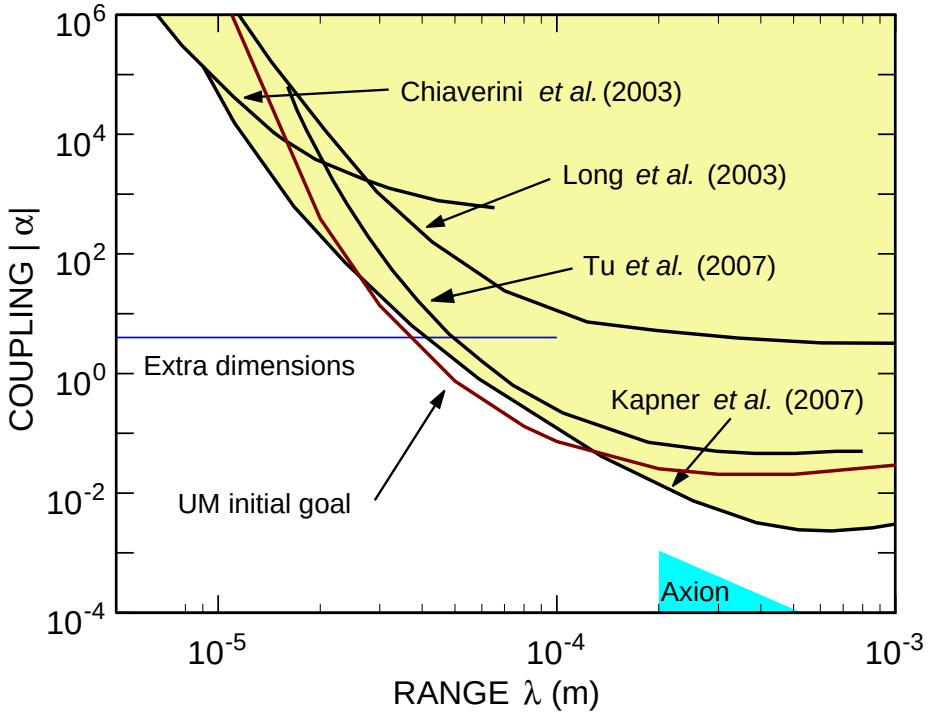

Figure 1.1: The initial sensitivity goal of the University of Maryland experiment (95% confidence) versus the existing limits.

The range of possible ISL violations due to the theory of extra dimensions [6] and the axion theory [7] are also shown, as well as the initial sensitivity goal of the University of Maryland experiment. The resolution goal of this experiment at 30 μm $< \lambda <$ 100 μm represents a slight improvement beyond the present limits [3].

1.1 Theoretical motivation

There are at least three important theoretical motivations to suggest that gravity might deviate from the ISL at sub-millimeter distance scales. Extra dimensions postulated to solve the hierarchy problem; the axion, a particle proposed as a solution to the strong CP problem; and the cosmological constant problem are discussed below.

1.1.1 Extra dimensions

The hierarchy problem in physics refers to the fact there appear to be two very different energy scales in nature − the electroweak scale and the Planck scale. The electroweak scale defined by the fine structure constant governs the unified electroweak interactions, while the Planck scale defined by Newton's constant G governs gravitational interactions. So far, we do not have a complete theory to explain why these widely separated energy scales seem to exist in nature.

The theory of large extra dimensions was proposed by Arkani-Hamed, Dimopoulos and Dvali [6] as a solution to the hierarchy problem without involving supersymmetry or technicolor. Their motivation was that, unlike the electroweak interactions, GR had not been experimentally tested from the scale of 1 mm to the Planck scale, which is a wide energy/distance scale spanning 33 orders of magnitude. They proposed a manifold with the four ordinary space-time dimensions plus n compact spatial extra dimensions of radius $\sim R$. Gravity alone propagates through these dimensions while the SM particles cannot.

Equating the $4+n$ dimensional mass scale to the four dimensional electroweak scale, one can infer the size of the extra dimensions. For $n = 1$, we get $R \sim 10^{13}$ cm, which would imply a deviation from $1/r^2$ to $1/r^3$ on solar system distance scales. For $n = 2$ extra dimensions, at distance scales less than $R \sim 0.1$ mm, the gravitational force law changes from $1/r^2$ to $1/r^4$.

In the last few years, two experiments seem to have also ruled out $n = 2$ case [3, 2]. The $n = 3$ case predicts $R \sim 1$ nm and R decreases further for greater n.

The Randall-Sundrum model [8] addresses the hierarchy problem by considering the universe to be a 3-brane embedded in a five non-compact dimensional space. In contrast to the idea of compact extra dimensions, they show that a five (or higher) dimensional case would be equally valid if the graviton were localized on the 3-brane using an appropriately tuned brane tension.

1.1.2 Axion

The strong CP problem in the SM refers to the fact that while the SM permits the violation of the combined symmetry operator of charge conjugation (C) and parity (P), no such violations have been found experimentally in strong interactions. The non-perturbative effects, which induce violations of P and CP, can be parameterized by a dimensionless angle Θ.

Peccei and Quinn [7] proposed an attractive resolution of this problem. One ramification of their theory is the existence of a new light-mass boson, the axion [9, 10]. The axion mediates a short-range mass-mass interaction. The upper bound

of $\Theta \leq 3 \times 10^{-10}$ corresponds to a violation of the ISL at the level of $\alpha = 10^{-3}$ at 200 μm. This is outside the reach of the current experiment but will be within the reach of our improved second-generation experiment [11].

1.1.3 Cosmological constant problem

Present observations favor an accelerating expansion of the universe. This implies a tiny but non-vanishing cosmological constant, which corresponds to a very small vacuum-energy density. This small value of the energy density is nearly impossible to explain from quantum field theory. This enormous discrepancy is referred to as the cosmological constant problem.

Sundrum [12] proposed that this could be solved if gravitons were 'fat,' which would lead to gravity being cut off at $\sim$ 20 μm; hence, the cosmological constant problem strongly motivates sub-millimeter range tests of gravity.

1.2 Review of the previous ISL experiment

An older version of this experiment was performed by Violeta A. Prieto [1, 13] in 2007. The experiment was carried out successfully, though it suffered from a number of technical flaws and a major design flaw. We will briefly describe the results of the experiment and the problems pointed out and recommendations made by the author.

The nominal test mass to source mass spacing was 180 μm and the presence of dust particles limited the source amplitude to 16 μm. Identifying the differential

mode acceleration of the test masses as a Yukawa type signal gave

$$\alpha = 240 \pm 320 \tag{1.2}$$

at range of $\lambda = 180$ μm.

There were several problems with this experiment, which resulted in a highly compromised sensitivity. Two of the dominant sources were high residual gas pressure and a design flaw.

The residual gas pressure in the experiment was very high due to a leak in the vacuum chamber. While other errors were dominant over the pressure-related error (possibly due to the small source amplitude), it is likely that the high pressure would have contributed to the total error. The use of an external pump to keep the pressure low also resulted in excess vibration.

The experiment suffered from a large error due to a design flaw. A soft link had been inserted between the test mass blocks and the rest of the detector housing in order to minimize source-driven distortions and to allow for alignment of the test masses. Inserting this soft link greatly increased the detector sensitivity to any source mass and detector coupling (such as through patch fields or residual gas pressure). The apparatus used also had an issue with a broken spring for one of the test mass blocks, which was a source for a random error.

A number of recommendations were made based on the results of the experiment. Some of the major ones are listed below:

1. Decoupling the source mass from the detector and suspending it separately. This also allows the source mass to be driven at resonance minimizing cross-

talk.

2. Holding the test mass block rigid against the rest of the housing and gold-coating relevant surfaces to minimize patch-field interactions.

3. Using niobium (Nb) test masses to avoid cooling to 1.7 K.

We implemented many of the suggested changes in the new experiment and performed some other modifications, which are described in detail in the following chapter.

Chapter 2

Design of the New Inverse-Square Law Experiment

The original design of the ISL experiment is described in detail in [1]. Fundamentally the design of the new experiment is the same − it employs a Newtonian null source and a superconducting differential accelerometer as the detector. However, several successive improvements to the design of the experiment were made over the course of two years, which ultimately led to a much more sensitive experiment. In this chapter, I will start by explaining the principle and the major hardware components of the experiment. In the later part of the chapter, I will discuss the errors and how some of these error mechanisms influenced key design changes in the experiment.

2.1 Principle of the experiment

To test the gravitational ISL to high precision, we need to bring two masses very close to each other, and measure the force between them as a function of their separation. Instead of measuring the absolute gravitational force, which is much harder to do, we modulate the position of one of the masses and measure its effect on the other. The heavier and moving mass is referred to as the source mass and the lighter mass (whose acceleration will be larger, thus easier to measure) is referred

to as the test mass.

A *null* test is one whose expected outcome is zero within its experimental errors. Searching for deviations from Newton's law becomes much easier if the Newtonian effect of the heavier mass is zero; i.e., if the source mass is a Newtonian null source. This is chiefly because it relaxes the tolerances on some of the physical dimensions of the source and test masses. Also, this reduces the dynamical range requirement of the detector, which may improve its sensitivity.

An infinitely long cylinder, an infinite slab or a hollow sphere (gravity is uniform inside) are examples of a Newtonian null source. For ease of implementation and best signal, a disk with large diameter to thickness ratio is a natural choice as a nearly null source in this experiment. Two test masses, instead of one, are symmetrically located on either side of the source mass. The motion of the test masses is sensed by pancake coils located behind them. The two sensing coils and a SQUID (Superconducting QUantum Interferometer Device) sensor are connected in a superconducting circuit and persistent currents are stored to make it a differential accelerometer.

If there exists a short-range force between the source and the test masses, then when the source is closer to one test mass, it is pulled (or pushed) towards the source mass. Thus, in one cycle of source mass oscillation, the distance between the test masses undergoes two cycles of oscillatory motion. As the source mass moves between the test masses, if Newton's law is violated, then the test masses experience a *second-harmonic* differential acceleration, which produces a current in the sensing circuit, which is in turn sensed by the SQUID.

As in any precision gravity experiment, the difficulty lies in the fact that the accelerations produced from gravitational forces are extremely small and comparable to the random accelerations of the test mass produced by statistical error sources such as thermal noise and amplifier noise. In addition, there exist several non-gravitational ways the source mass could affect the test masses. These constitute the systematic errors in the experiment.

To get an idea about how weak the gravitational effect is, we can do a quick calculation to find the effect on the test masses due to a Yukawa potential of strength $\alpha = 1$ and range $\lambda = 100$ μm. The differential acceleration produced due to the maximum source amplitude of 130 μm is $\sim 1 \times 10^{-11}$ m s^{-2}, which corresponds to a test mass displacement amplitude of about 1×10^{-15} m. With the ultimate sensitivity of the detector (amplifier and thermal noise limited), we would be able to detect the above signal to one part in 1000 with an integration time of 10^6 s. Another way of stating the above is that we would ultimately be sensitive to a test mass amplitude of $\sim 1 \times 10^{-18}$ m!

2.2 Experimental hardware

2.2.1 Newtonian null source and test masses

The source mass is a circular disk of large diameter to thickness ratio, just as in [1]. As explained above, it approximates an infinite plane slab, which is a Newtonian null source, as compared to the thin and smaller test masses. Figure 2.1, which is an expanded cross-section of the experiment, illustrates the configuration

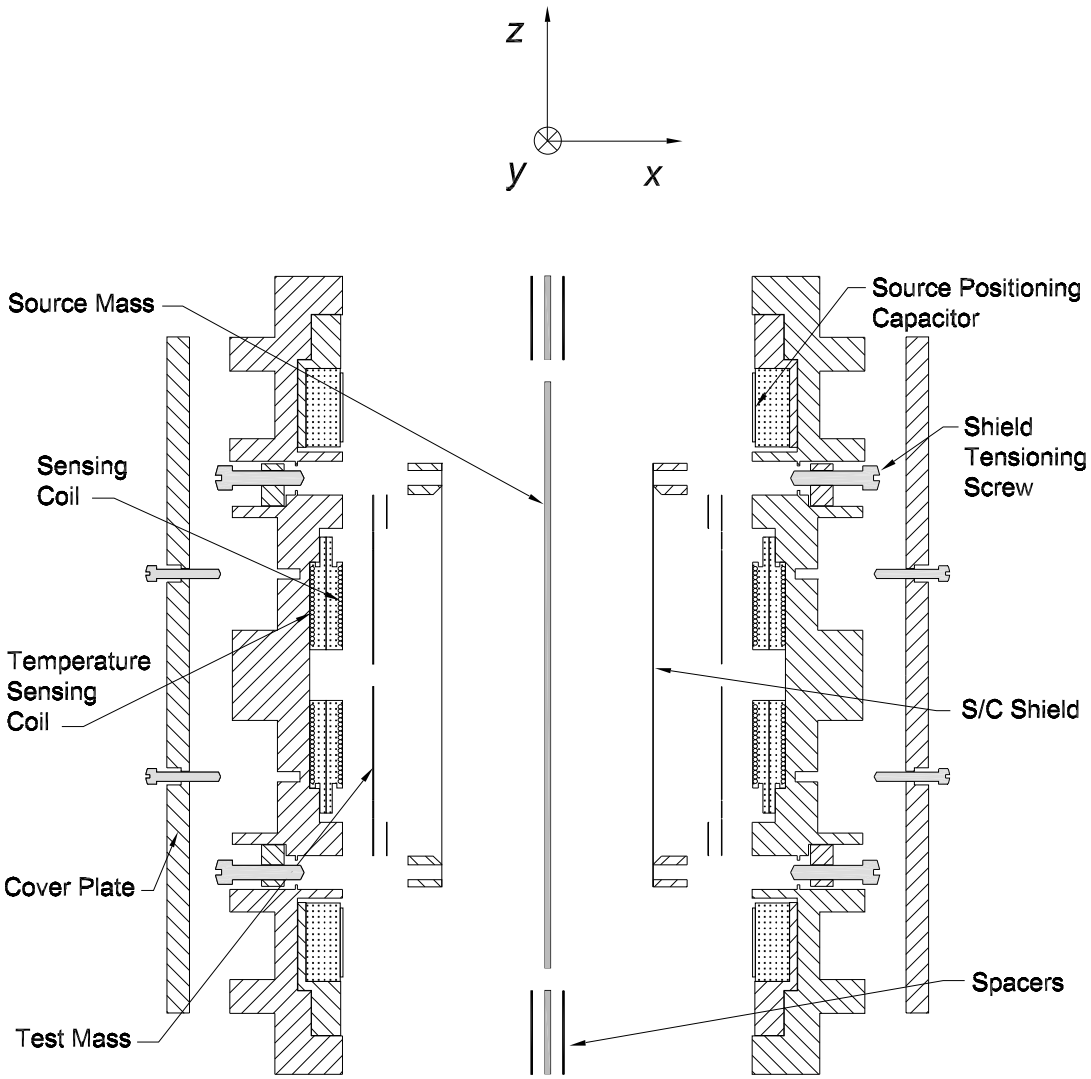

Figure 2.1: Expanded cross-section of the experiment.

of the source and test masses with their associated coils (the axial dimensions are exaggerated for clarity). The source mass had a diameter of 0.165 m, thickness of 2.90 mm, and a mass of 531 g.

The (laboratory) coordinate system used throughout this thesis is also shown in Fig. 2.1. The z axis is vertical. The sensitive axis of the detector is aligned along the horizontal x axis.

A Nb source mass had been prepared as a second source mass for the original experiment [1]. In the original design, the source mass was driven magnetically by an alternating current (AC) through a coil with persistent current stored in it, thus it needed to be superconducting itself. Ta has a superconducting transition temperature of about 4.5 K, thus the experiment was performed at about 1.7 K. A Nb source mass would eliminate the need to reduce the temperature of the experiment to 1.7 K, which was a difficult and problematic process.

In the new design, described in detail below, the source mass was suspended separately from the housing. It was driven *at resonance* by external coils and a bar magnet attached to its suspension. Thus, there was no need for a superconducting source mass in the new design. However, we chose to use the already available Nb source mass in the interest of saving time. In hindsight, this led to the issue of cross-talk between the source and the sensing circuit, which increased the measurement error.

The Nb source mass had been polished using 'double disk grinding' to less than 3-μm surface variations on either side and a surface map of the thickness variations had been made. Based on the recommendations of [1, 14, 15] to minimize patch-field

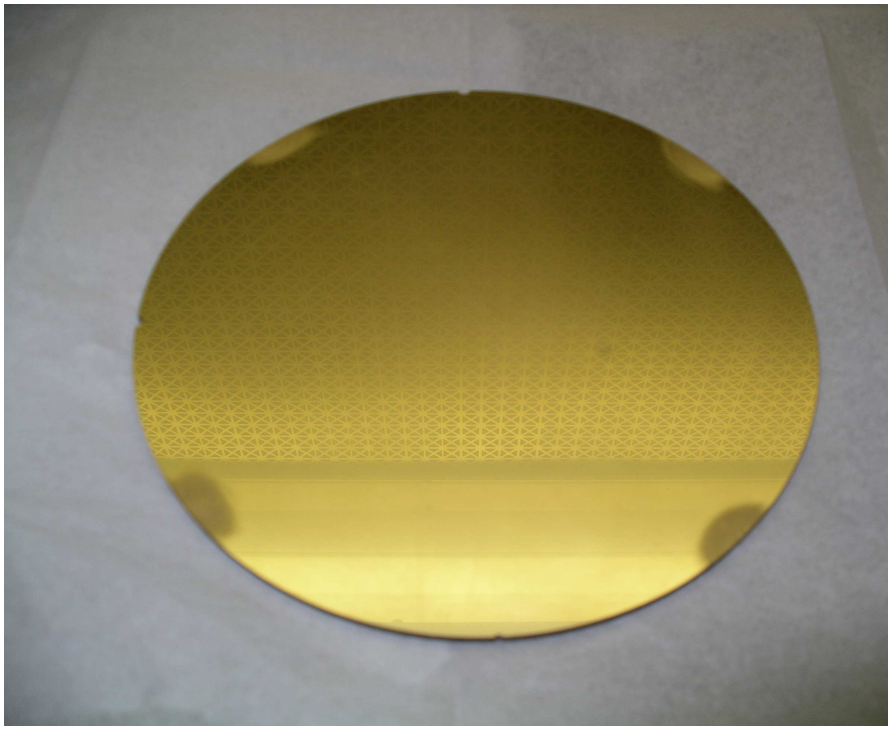

Figure 2.2: Gold-coated Nb source mass.

forces, we deposited a 100-nm layer of gold on both surfaces of the source mass by physical vapor deposition (PVD) technique (see Fig. 2.2).

We also replaced the Ta test masses of the original experiment with Nb test masses of identical dimensions, to allow operation at 4.2 K. The test masses had a diameter of 71 mm, thickness of 240 μm, and a mass of 8.7 g each. The total mass of the housing excluding the source mass and the test masses was 19.8 kg.

2.2.2 Source and detector suspension

As described in [1], the motion of the source mass, whose rim was clamped between the two halves of the detector, created severe distortion of the housing.

To compensate for the tilt of the detector, tilt sensing by the laser tilt meter and feedback via the voice coils had to be applied to the suspension wires. Furthermore, as the source was not being driven at resonance, the nonlinearity of the source drive and suspension become important error sources. To avoid these complications, we decided to separate the detector from the source and suspend them from different locations altogether.

Our initial approach was to suspend the detector from the top of the vacuum can and the source from the top of the cryostat insert in order to achieve a sufficiently low fundamental frequency for the source mass. Without making significant changes to the cryostat insert, it seemed reasonable to use the old detector suspension cables to suspend the source and to create a new way of suspending the detector from the top of the vacuum can using stainless steel wires. However, the higher suspension frequencies for the detector resulted in reduced vibration isolation for the detector. This caused the test mass modes to ring up to large amplitudes, which caused the differential-mode SQUID to overload at the currents required for full sensitivity. Therefore, we modified the suspension scheme to have both the source and the detector suspended from the top of the cryostat.

For the detector, we went back to the original design, as shown in Fig. 2.3. The rubber tube provided some vibration isolation and damping along the vertical. The voice-coil actuators were used for common-mode calibration described in the next chapter. The source rim, to which the source was originally connected by the cantilever springs, was cut away using electric discharge machining (EDM) into four parts, as shown in Fig. 2.4. This created a passageway for the source suspension

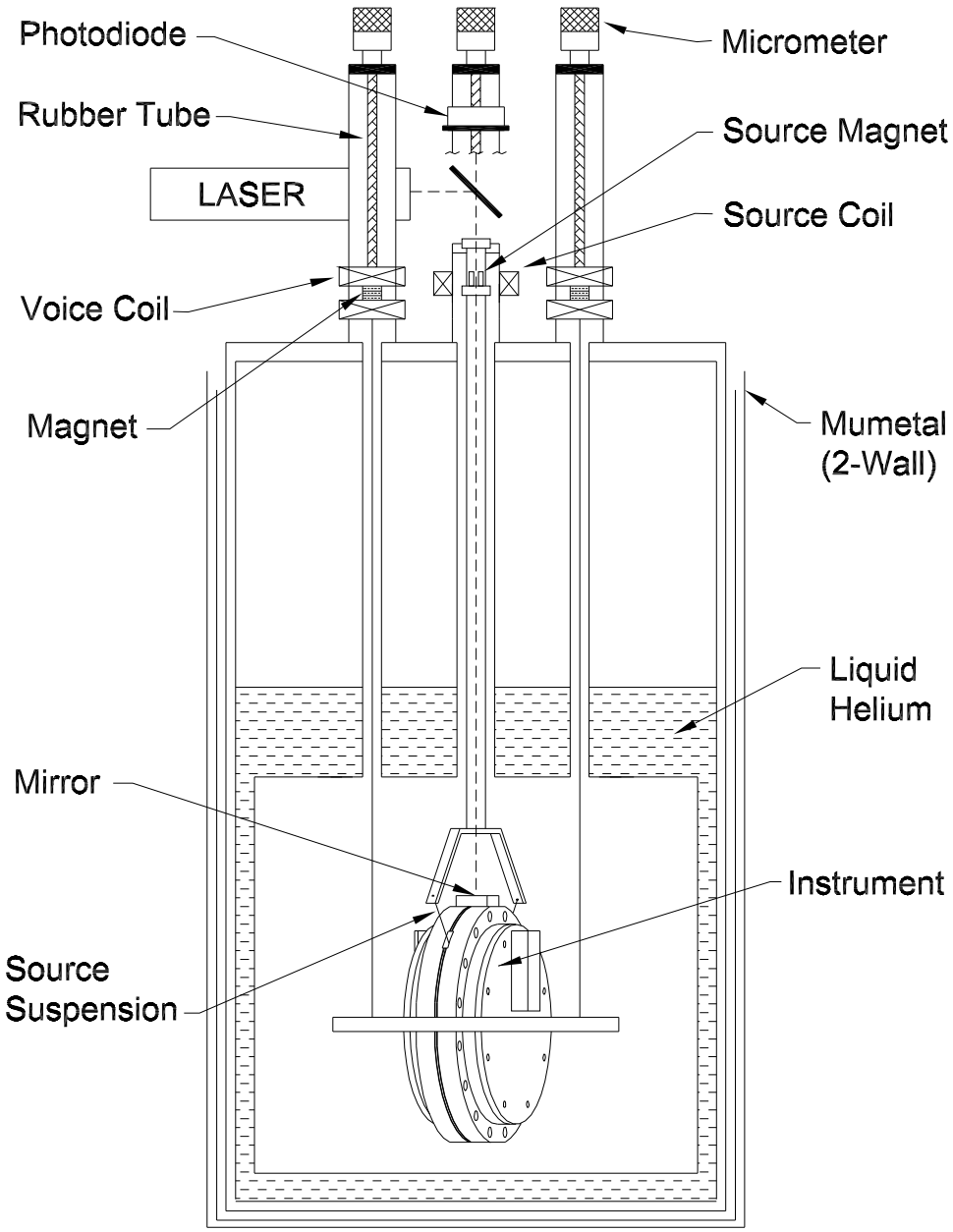

Figure 2.3: Schematic of the test cryostat.

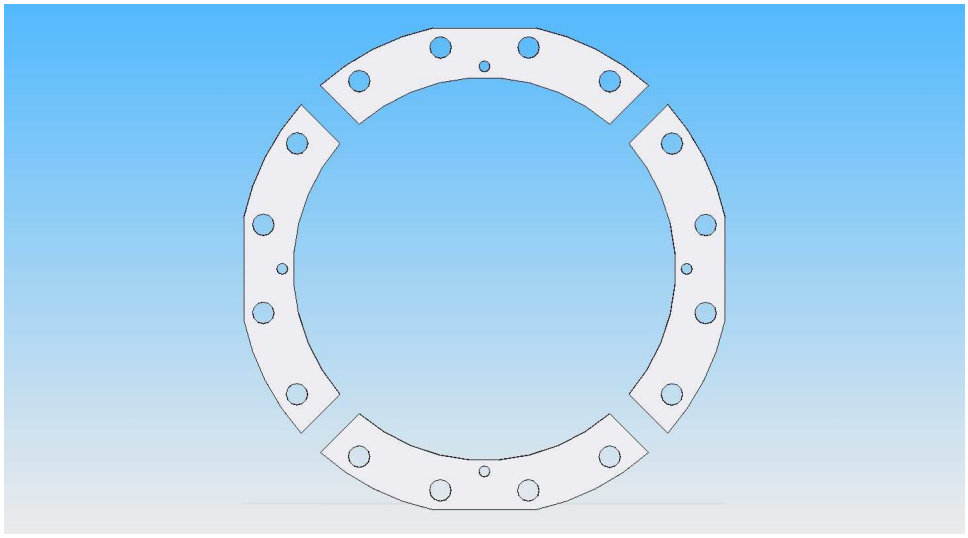

Figure 2.4: Spacers formed out of the previous source rim.

wires.

Figure 2.5 shows the source suspension scheme. The source had four 0-80 UNC threaded holes machined into it at 90 degrees each. A 0.040-inch diameter hole was drilled into a 0-80 UNC brass screw and a hex was machined on its head. A 0.024-inch diameter phosphor bronze (PhBr) wire was soldered into the brass screw and it was screwed into the source mass.

On the other end, the wire was soldered to a 0.75-inch long, 10-32 UNC threaded rod made of brass. This was then attached to an aluminum (Al) structure, as shown in Fig. 2.5, with the help of two brass nuts and washers. Two copper (Cu) springs are then attached between the Al structure and the cryostat frame. These springs force the two modes of the pendulum to split. Consequently, the frequency of the undesired mode of the source mass moving sideways was increased to 0.6 Hz, while the frequency of the source mass oscillating along the x axis increased only

to 0.47 Hz. They also serve as heat-sinks to keep the source close to the detector temperature.

The Al structure was supported by two 0.015-inch diameter PhBr wires. Figure 2.6 shows how these wires are secured at the top. It also shows a cylindrical brass piece, which has two permanent bar magnets glued to it. These are used to drive the pendulum mode of the source mass at resonance with the help of the source driving coil located outside as shown. A transparent window was mounted at the top of the brass fixture, to allow passage for a laser beam (part of an optical lever for tilt readout described later).

2.2.3 Shields

The shields in [1] were prone to damage after a few cool-down cycles. Therefore, we decided to use a 25-μm Nb foil instead of the 12.5-μm foil used previously. However, it proved difficult to bond them reliably to the shield rims (diffusion bonding was used previously). Instead, we were able to attach them to the rim using many spot-welds made using a Miyachi Unitek dual-pulse resistance welding power supply. They were then coated with a 100-nm thick layer of gold to minimize patch-field type interactions with the source (see Fig. 2.7).

Once the shields were attached securely to the rims, they were located over the test mass block, as shown in Fig. 2.1. They were then stretched taut by using the shield tightening screws as shown. This is a rather delicate process and too much tension can cause the shields to tear. Too little, and the shield may be distorted

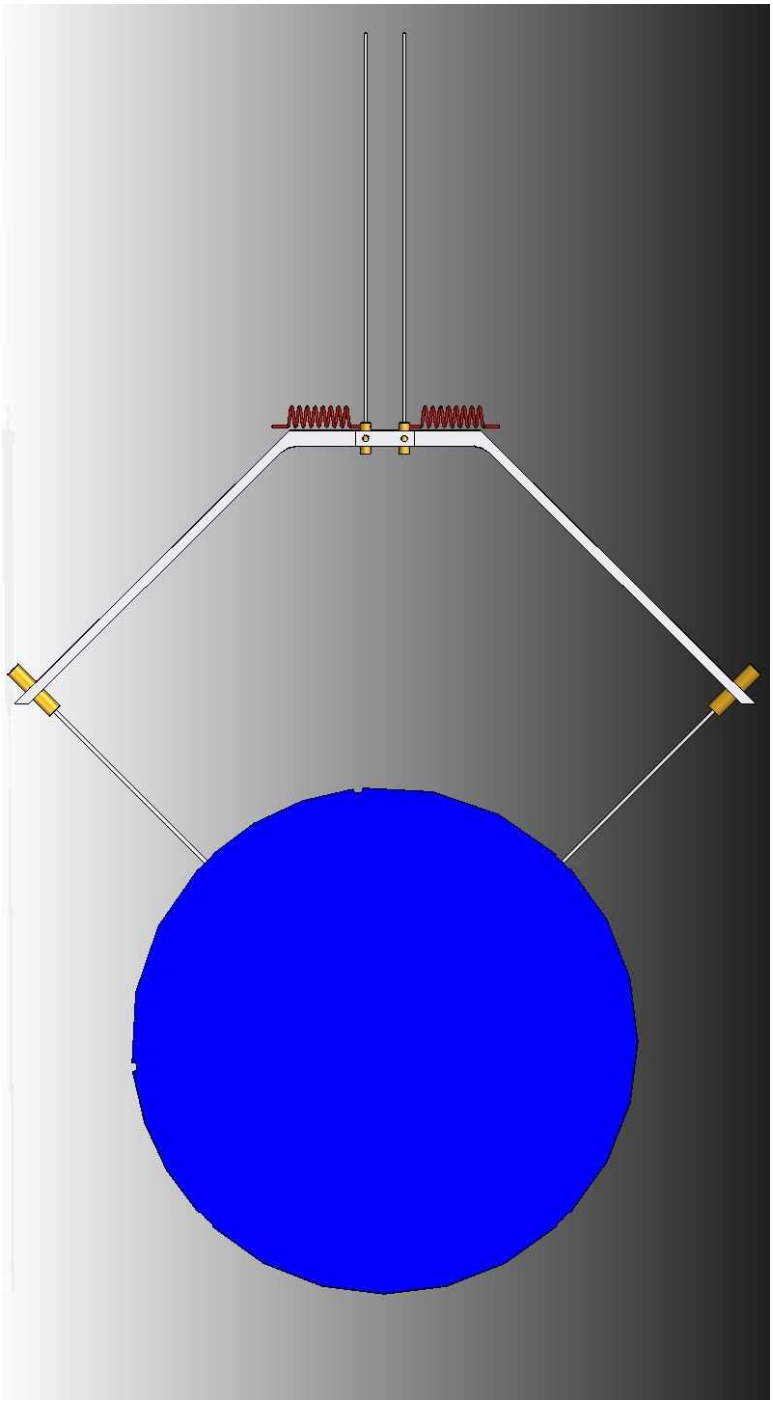

Figure 2.5: Source mass suspension schematic.

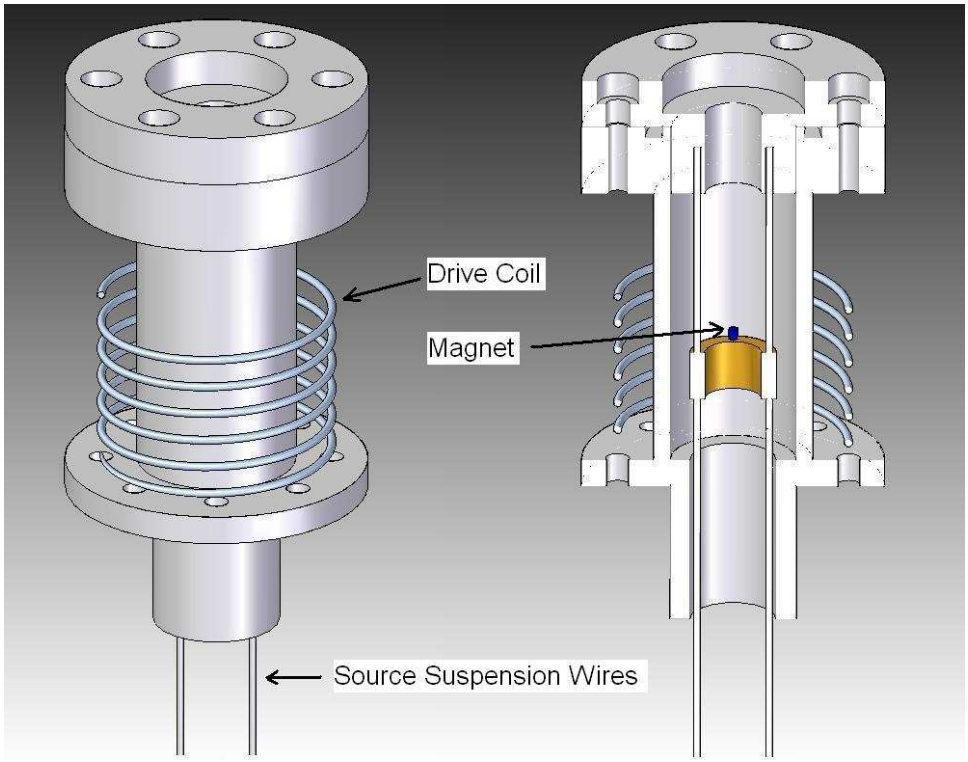

Figure 2.6: Fixture mounted on cryostat as part of the source mass suspension.

causing it to stick out. It might also have too low a resonance frequency, which would result in a large response to source motion (through pressure or other couplings). This would in turn affect the test masses and would thus create a systematic error. We were able to use a torque wrench to apply a uniform torque of 3 inch-pound to all the shield tightening screws.

2.2.4 Capacitor plates

The capacitor plates used in the original experiment were found to be extremely useful. This is even more so the case in the new design. They are vital in being able to free the source mass and in positioning it. Also, they are the

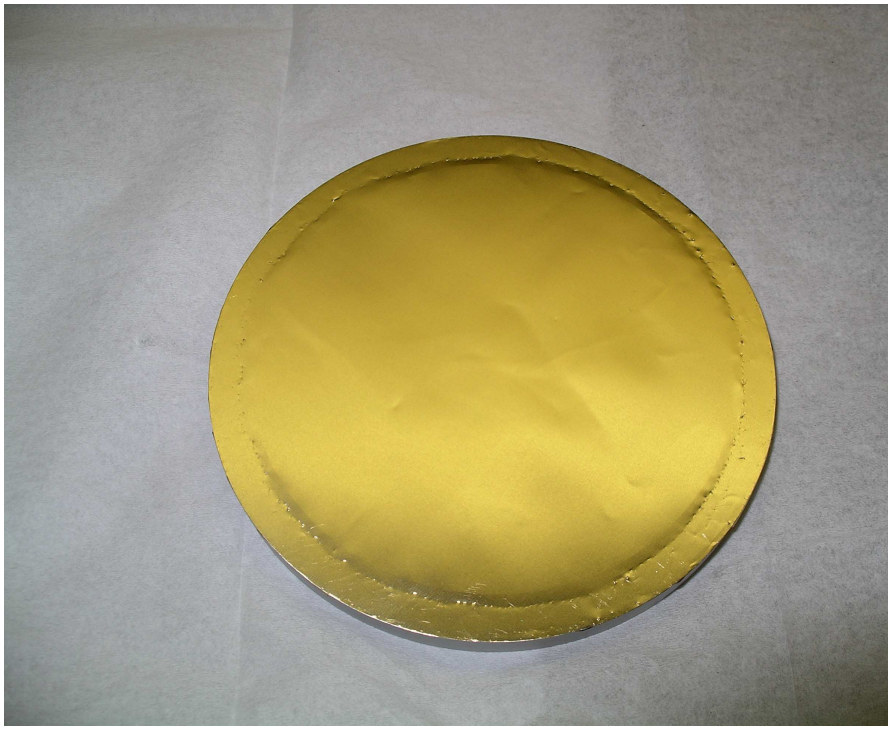

Figure 2.7: Gold-coated Nb shield.

only means of measuring the source amplitude. Due to their crucial role in the experiment, we decided to increase their area as much as possible.

As the source driving coils were no longer necessary, we used the coil forms to hold four pieces of Nb to act as capacitor plates, as shown in Fig. 2.8. The capacitor plates were cut out of 125-μm thick Nb foil, glued to a Macor back plate and lapped. Just as the shields and the source mass, the capacitor plates were also coated with a 100-nm thick layer of gold.

The capacitor plates were positioned so that they would be coplanar with the shields and the rim of the housing. This was done with the help of several Nb spacers placed behind the plates. A measurement of their depths from the outer edge of

Figure 2.8: Capacitor plates with gold-coating.

the housing was then made with a depth gauge to confirm their location. Thus the mean gap between any capacitor plate and the source mass was ~ 200 μm.

2.2.5 Sensing circuits

The sensing coils used in this experiment were the same as used in [1], and work on the principle described in [16]. Persistent currents are stored in the sensing circuits, as shown in Fig. 2.9(a) and (b). The inductance of the sensing coils depends on the spacing of the test masses from the coils. Thus, the test mass motion modulates the inductance, which in turn modulates the current stored in the circuit.

The two test masses moving together in the same direction (in phase) is termed as common-mode (CM) motion. If they move in opposite directions (out of phase,) the motion is said to be in differential mode (DM). If inductances L_{D1} and L_{D2} in Fig. 2.9(a) were equal, and the coils and test masses were perfectly matched, then storing current in the configuration shown with $I_{D1} = I_{D2}$ (referred to as *parallel* current) would make the SQUID sensor sensitive only to DM. Likewise, if inductances L_{C1} and L_{C2} in Fig. 2.9(b) were equal, and the coils and test masses were perfectly matched, then the currents shown with $I_{C1} = I_{C2}$ (referred to as *series* current) would make it sensitive only to CM.

In reality, we store a large amount of *parallel* current and a small amount of *series* current (to tune out the mismatch) to obtain maximum sensitivity to DM motion. Even so, the CM rejection (along the x axis) is finite and is on the order of 10^4 or more (based on the current resolution). For the CM circuit, we simply store the *series* current alone, since DM motion is typically several orders of magnitude smaller. Thus the CM output is dominated by CM motion along the sensitive axis (x axis).

The dynamics of the test mass motion and the sensitivity of the differential accelerometer are described in great detail in [1]. Where required, we will quote the results from [1] without derivation.

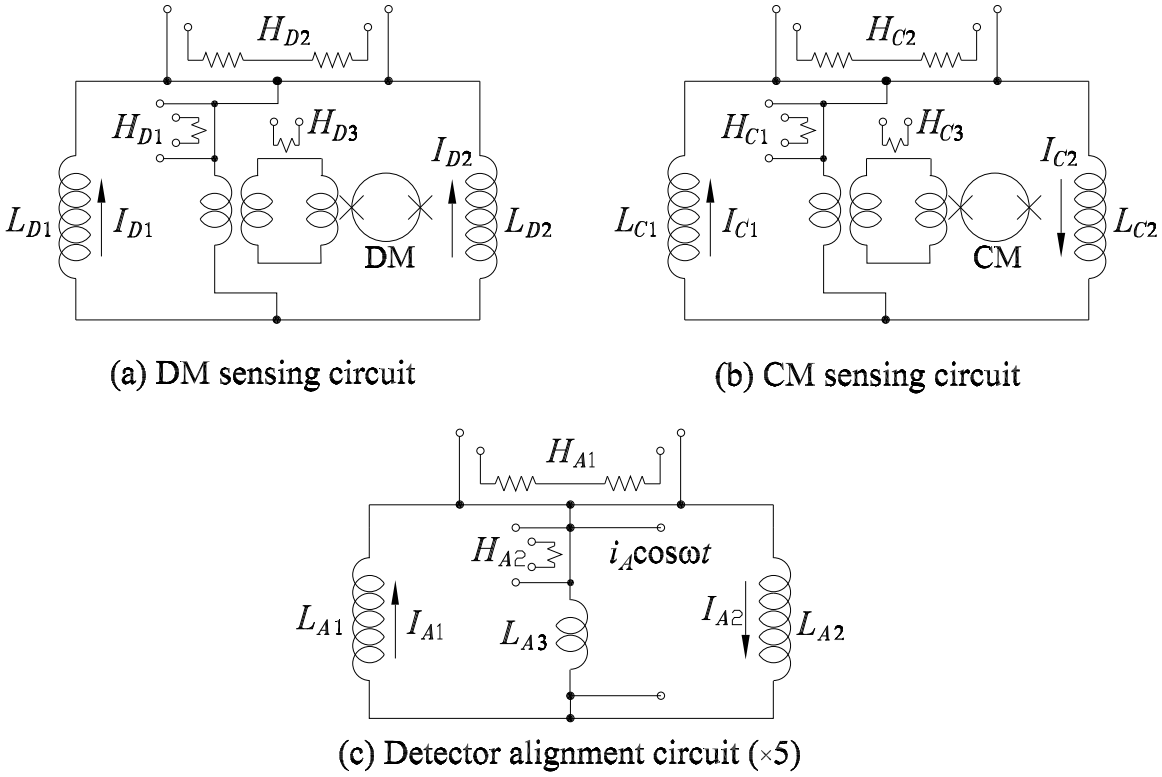

Figure 2.9: Sensing and alignment circuits used.

2.2.6 Alignment circuits

In the initial design, four alignment coils were placed behind the test mass blocks, so as to be able to better orient the test masses with respect to each other. This allowed the DM output to achieve a CM rejection of better than 1 part in 10^4. However, this design was a major shortcoming of that experiment, as discussed in Section 1.2. It allowed any interaction between the source and the housing to produce differential accelerations on the test masses, thus producing large DM signals.

By making the test mass blocks rigidly fixed to the housing, we overcame the above mentioned flaw. But unfortunately, we were limited to whatever alignment

the test masses had when they were installed. In other words, there was no way to correct for the misalignment of the test masses.

In order to measure and characterize these errors, we would have to shake the detector linearly along the x, y, and z axes, and rotate it about y and z, and possibly about x. Also, it was crucial to align the source mass with respect to the detector to within 10^{-4} rad in order to maximize the source amplitude. Thus, to meet both of these requirements, we designed a set of five alignment circuits to position the detector along all six degrees of freedom.

The layout of the alignment circuit is very similar to that of the sensing circuit and is shown in Fig. 2.9(c). A schematic of the arrangement of the alignment coils around the detector is shown in Fig. 2.10. The complexity of the wiring and assembly were substantially increased.

2.2.7 Laser tilt meter

As explained in [1], the experiment uses an optical lever arrangement to measure the tilt of the detector. A 1-W laser is passed through a partially reflecting mirror and sent down the central tube. It is bounced off a mirror mounted on the detector and falls on a photo-sensitive diode (PSD). The output of the PSD is fed into a junction box, which gives out the x, y position of the reflected beam. The PSD is mounted on a x-y table with micrometers to control its position.

To calibrate the laser readout, we move the PSD along the x axis by a fixed

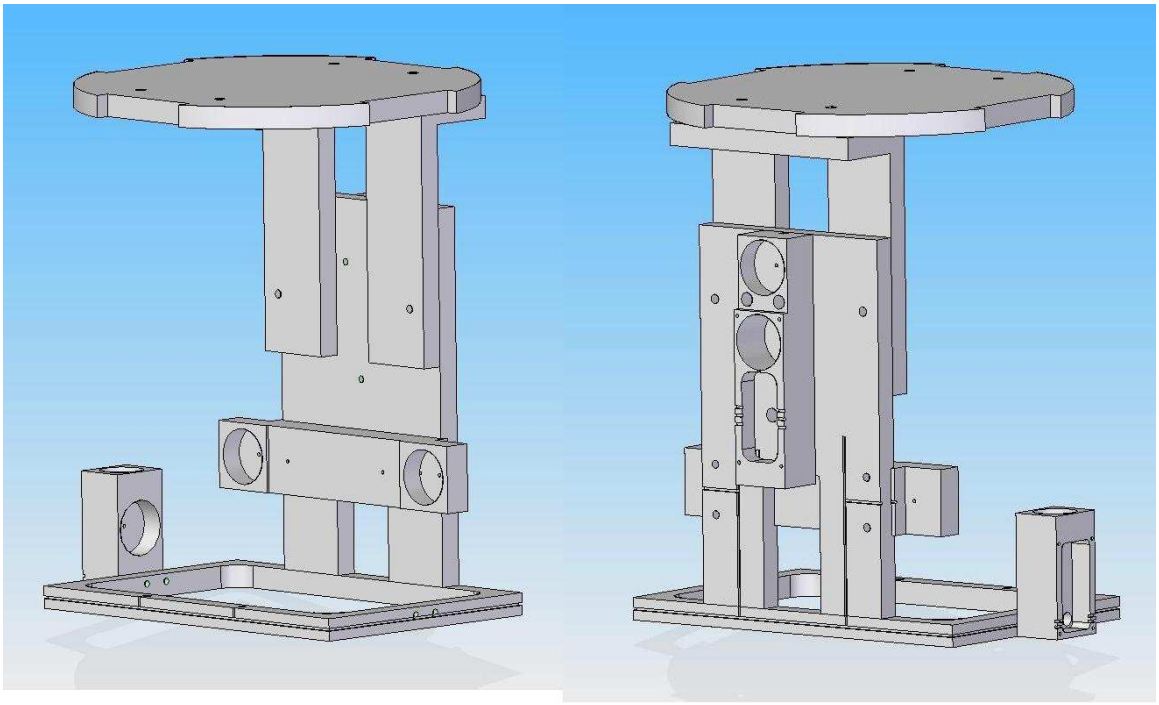

Figure 2.10: Configuration of the alignment coils, front and back view. Only one out of a pair of symmetrically located coil holders are shown.

distance δx and along the y axis by the same distance, and record the change in the x and y outputs of the junction box. From basic trigonometry, the detector tilt sensitivity or transfer function of the laser is then given by

$$H_{tilt} = \frac{\delta x}{2L}\frac{1}{V_{out}}\text{rad/V}, \tag{2.1}$$

where L is the distance between the location of the PSD and the mirror, and V_{out} is the corresponding measured voltage difference.

2.3 Expected Yukawa signal

Using Eq. (1.1), we can estimate the Yukawa signal for the source-test mass geometry. The signal is shown in Fig. 2.11 as a function of the source mass amplitude for two different length scales and strengths of a violation signal. For reference, we also plot the Newtonian error signal produced from the finite radius of the source mass. As seen from the figure, it is well below any potential signals we hope to detect.

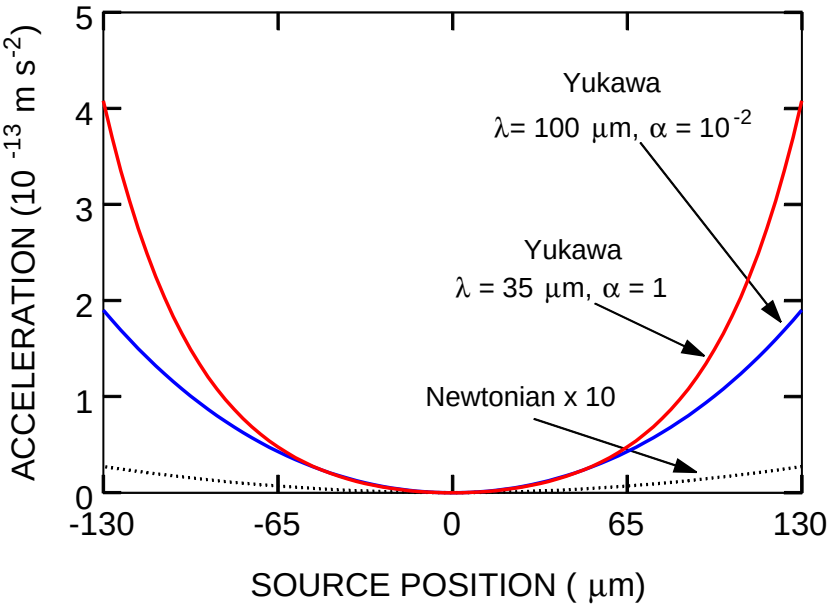

Figure 2.11: Newtonian and Yukawa signals versus source position.

2.4 Expected sensitivity

Understanding and anticipating the experimental errors is extremely important to any precision experiment. We examined many of the important sources of error in our experiment, both statistical and systematic. However, as is often the case, we discovered some unexpected sources of error, which were dominant. I will discuss these in more detail in the next chapter, and summarize below the errors we investigated before our final cool-down.

2.4.1 Metrology error

By making the Newtonian force from the source mass negligible, we had made the experiment insensitive to test mass metrology. Thus, the requirement for metrological precision rested on the source mass. We considered the thickness variation of the source mass as the chief metrology error. Prieto [17] and Chen [18] have shown using two different calculations, based on the measured surface height map of the current source mass (both sides), that the source mass used in the experiment would have a Newtonian acceleration from the thickness variation at the level of $\sim 1 \times 10^{-15}$ m s^{-2}, which is two orders of magnitude smaller than our sensitivity requirements.

2.4.2 Intrinsic noise

The intrinsic power spectral density (PSD) of a superconducting differential accelerometer can be written [19, 20] as

$$S_a(f) = \frac{8}{m}\left[\frac{k_B T \omega_D}{Q_D} + \frac{\omega_D^2}{2\eta\beta} E_A(f)\right], \tag{2.2}$$

where m is the mass of each test mass, $\omega_D = 2\pi f_D$ and Q_D are the DM (angular) resonance frequency and quality factor, β is the electromechanical energy coupling coefficient, η is the electrical energy coupling coefficient of the SQUID, and $E_A(f)$ is the input energy resolution of the SQUID.

For our experiment, $T = 4.2$ K, $m = 8.7$ g, $f_D = 13$ Hz, $Q_D = 10^5$, $\eta = 0.25$, $\beta = 0.2$, and $E_A(f) = 1 \times 10^{-30}\ (1 + 0.1\text{Hz}/f)$ J Hz^{-1} for the commercial dc SQUID used. This gives $S_a^{1/2}(f) = 1.2 \times 10^{-11}$ m s^{-2} Hz$^{-1/2}$ at $f = 0.94$ Hz.

2.4.3 Seismic noise

Being a low-frequency experiment, seismic or ground noise is a major error source. The experiment frequency is 0.95 Hz, which is only a factor of 2 or so above the linear resonance frequencies of the detector suspension, thus it does not provide significant vibration isolation.

The way in which seismic noise couples to the DM output has been described in detail in [1, 21]. We will briefly summarize the chief result below. If $\vec{r}$ is the position of the test mass of one accelerometer with respect to the platform, and $\vec{r}_M$ and $\vec{\Omega}$ the position and angular velocity of the platform with respect to the inertial reference frame, the DM acceleration due to misalignment can be given as

$$a_{d_{misalign}} = -l(\vec{\Omega}\cdot\hat{n})(\vec{\Omega}\cdot\delta\hat{l}) - l\hat{n}\cdot(\dot{\vec{\Omega}}\times\delta\hat{l}) + \delta\hat{n}\cdot(-\ddot{\vec{r}}_M + \vec{g}), \tag{2.3}$$

where l is the baseline of the accelerometer (the distance between the centers of the test masses), $\hat{n}$ is the mean accelerometer sensitive axis, $\delta\hat{l}$ is the misalignment between the baseline axis and the mean sensitive axis, and $\delta\hat{n}$ represents the misalignment between the sensitive axes of the two test masses. Thus, the two types of misalignments have two different effects. $\delta\hat{n}$ generates DM sensitivity to vibration and to the local gravity acceleration. On the other hand, $\delta\hat{l}$ causes the differential accelerometer to be sensitive to angular acceleration (produced by seismic noise or otherwise). In addition, $l\delta\hat{l}$ can be visualized as misconcentricity between the two test masses.

The CM acceleration noise due to linear seismic noise density was estimated to be $\sim 1\times10^{-7}$ m s^{-2} Hz$^{-1/2}$ [20]. With an estimated CM rejection of 1 part in 1000 along the x axis and a misalignment of 1 part in 1000 along the y and z axes, the noise level at the DM output due to the rms sum of linear seismic noise along three orthogonal directions would be

$$a_d^{\delta\hat{n}} = 1.73\times10^{-10}\ \text{m s}^{-2}\ \text{Hz}^{-1/2}. \tag{2.4}$$

Using the data from previous measurements made in our laboratory [22], the angular acceleration noise density is found to be $\sim 3\times10^{-8}$ rad s^{-2} Hz$^{-1/2}$. Estimating a misconcentricity $l\,\delta\hat{l} = 500$ μm, the noise density due to the rms sum of angular accelerations along two orthogonal degrees of rotation would be

$$a_d^{\delta\hat{l}} = 1.50\times10^{-11}\ \text{m s}^{-2}\ \text{Hz}^{-1/2}. \tag{2.5}$$

Seismic noise (linear) was thus our largest expected source of random error. The measured noise floor in the experiment, discussed in the next chapter, was very close to the theoretical prediction.

2.4.4 Pressure-mediated coupling

A pressure-mediated coupling was discovered in a cool-down performed in August 2008. This was found to be about four orders of magnitude higher than the ultimate noise floor we were aiming for and had not been anticipated previously. It was thus the single most important error source to overcome before we could perform the experiment.

The discovery of the error and the steps taken to understand and overcome it are described in Appendix A. Assuming the pressure in the chamber is $\leq 1 \times 10^{-7}$ torr, the expected DM acceleration signal is $\leq 1 \times 10^{-13}$ m s^{-2}.

2.4.5 Magnetic cross-talk

With the pressure of the chamber sufficiently lowered, we performed another cool-down of the experiment in April 2009. Unfortunately, we discovered another very significant source of error. There was a source motion dependent signal in the SQUID output even when there was no sensing current in the circuits. This implied that there was magnetic cross-talk between the source and the sensing circuit and/or between the source and the SQUID sensors.

The detailed description of the problem is given in Appendix B. We employed

various techniques to overcome it and it was eventually reduced by close to two orders of magnitude. During the experiment, we came up with another technique to reduce the cross-talk error still further.

2.4.6 Electrostatic forces

There are two main types of electrostatic forces which can provide additional coupling between the source mass and the detector housing:

1. Contact potential differences (CPD),

2. Surface potential variation (also called 'patch effect').

When two metals are placed in contact with each other, a potential difference can appear between them due to differences in the work function of the metals. This is known as 'contact potential difference'.

The surface of a polycrystalline metal is normally composed of patches with different crystallographic orientation. This can lead to a position-dependent potential difference between any two metal surfaces, known as 'patch effect'. In addition to the crystallographic orientation, contaminants, adsorption layers, or temperature differences can affect the patch potential distribution and magnitude [23, 24, 26].

All together, the two effects produce a significant surface potential difference between the source and the detector. Speake [24, 25] suggests that the mean of the potential differences between a pair of parallel plates can be eliminated by using a voltage bias. In the case of our experiment, the source mass is suspended between two sides of the housing. Each side facing the source mass contain four separate

capacitor plates and a shield. Furthermore, the source mass is grounded through its suspension wires and the Cu springs whereas the housing is grounded through its own suspension cables and its heat-sinks. Thus the situation is much more complicated, and it is unclear if the interaction can be reduced by applying a bias voltage to the source or not.

Before the cool-down, we did a rough estimate of the magnitude of patch effect forces. As shown in [24], based on the size of the crystals on the surfaces and the gaps involved, the force between them can be formulated into two types:

1. For surfaces where the crystal or patch size is small compared to the gap, the force per unit area can be expressed as

$$F_p(d) = -\frac{2\epsilon_0\sigma_\nu^2}{k_{max}^2 - k_{min}^2}\int_{k_{min}}^{k_{max}} \frac{k^3}{\sinh^2 kd}\, dk, \tag{2.6}$$

   where d is the gap, σ_ν is the standard deviation of the voltage distribution, and the wave numbers $k_{max,min} = 2\pi/\lambda_{min,max}$ are related to the maximum and minimum sizes $\lambda_{max,min}$ of the crystallites [27].

2. For surfaces where the patch size is much larger than the gaps, the force per unit area is expressed as

$$F_p(d) = -\frac{\epsilon_0(v_1 - v_2)^2}{2d^2}, \tag{2.7}$$

   where $v_1 - v_2$ is the difference between the mean electrode voltages.

As we had deposited a 100-nm layer of gold on the Nb surfaces, we made the initial assumption that we were dealing with the former case. In such a scenario, as

the source moves along the x axis in its fundamental pendulum mode at an amplitude of 130 μm and the total gap between the housing and the source is 200 μm, the force on the housing would be about $F_p = 1.0 \times 10^{-12}$ N. Thus the CM acceleration signal at the fundamental would be

$$a_p(d) = -\frac{F_p}{M_p(\omega_x^2 - \omega_s^2)} = 2.0 \times 10^{-14} \text{ m s}^{-2}. \tag{2.8}$$

There are several ways that this signal could appear at the second harmonic, such as nonlinearity (of the sensing circuit), asymmetry, etc., all of which tend to produce a significantly smaller second harmonic. As the fundamental signal was already so small, the second harmonic was thus considered insignificant. Later, we learned that patch effect can be dominated by contamination from impurities [23, 27, 28]. From the experimental data, we suspect that this was indeed the case. It is then likely that Eq. (2.7) was more suitable to explain the interaction.

2.4.7 Casimir force

In quantum electrodynamics (QED), the presence of conducting surfaces (which affect boundary conditions in solving Maxwell's equations) can modify the description of the vacuum state. The surfaces can limit the allowed electromagnetic modes thus altering the ground state of the electromagnetic field. Thus their movement produces a change in net energy. This is equivalent to a force between the surfaces and is known as Casimir effect [29].

The Casimir force between two perfectly parallel and conducting plates is

$$F(d) = \frac{\pi^2 \hbar c A_p}{240 d^4}, \tag{2.9}$$

where c is the speed of light, $\hbar$ is the reduced Planck constant, A_p is the surface area of the plates, and d is the distance between them.

For a source mass amplitude of 130 μm and a gap of 200 μm, the expected error due to Casimir force at the the second harmonic was $a_d(2f) = 1.32 \times 10^{-17}$ m s^{-2}, which was negligible.

2.4.8 Summary

The errors estimated before the actual cool-down of the experiment are summarized in Table 2.1. We estimated that we would collect 10^6 s of data during the experiment. While the random noise will be reduced by averaging, the systematic errors will not. We expected the residual gas pressure and the seismic noise to be the dominant sources of error. The sensitivity (2σ) limited by twice the total estimated error 2.0×10^{-13} m s^{-2} is plotted in Fig. 1.1 as the UM initial goal.

Error source	Level ($\times 10^{-14}\,\mathrm{m/s^2}$)
Metrology	< 0.1
Intrinsic noise (10^6 s averaging)	1.2
Seismic noise (10^6 s averaging)	17
Residual gas pressure	< 10
Magnetic coupling	< 0.1
Electrostatic coupling	< 2
Total	20

Table 2.1: Total error budget for source to test mass spacing of 280 μm, source to shield spacing of 210 μm, and a source displacement of $\delta d = 130$ μm.

Chapter 3

Experimental Setup and Calibration

In this chapter, I will describe the procedure followed for the final cool-down of the experiment, in August 2009 through January 2010, and also explain the various calibration measurements made to characterize the detector.

3.1 Cool-down procedure

The cool-down procedure followed for this experiment is very similar to the one described in [1]; however, there were some important changes.

The most important step in the setup procedure is the room-temperature positioning of the source with respect to the detector. We start by adjusting the detector height (and the source height, if necessary) to locate the source roughly at the center of the detector. The detector is then aligned crudely to be vertical with the help of a spirit gauge. If required, we then adjust the position of the alignment coils so that they are all evenly spaced about the detector. Then, we make finer adjustments relying on the capacitance plates in order to make the source and detector aligned about the y axis. Next, we make adjustments to the source alignment and position about the vertical and the x axis, respectively, using the Cu springs, as shown in Fig. 2.5. This final adjustment is very crude and it takes

several attempts before the source is freed and positioned at the center.

Once the source-detector position has been set, the spirit gauges mounted on the cryostat are adjusted to read zero and the laser is turned on. We then adjust the mirror so that the laser beam is reflected back to the center of the PSD. The mirror holder is mounted on top of the detector using four titanium (Ti) screws and a thin ring of soft indium (In) is placed between them. Thus, the mirror inclination can be adjusted by selectively compressing the In on one side or the other.

After checking all the electrical connections, the chamber is then sealed using an In seal. The insert is then leak-tested using the helium (He) leak-detector (Leybold-Heraeus Ultratest-F). The insert is then moved into the dewar and the tilt of the dewar is adjusted until the spirit gauges on the cryostat read zero again. The charcoal getter is then raised to a temperature of $\sim 70°C$, and the chamber is pumped continuously for about 48 hours.

We then transfer dry He gas into the chamber, raising the pressure to ~ 30 torr. Liquid nitrogen (N_2) is then slowly transferred into the dewar and allowed to collect well over the chamber. Its contents slowly cool to 77 K over a period of 24 hours. The N_2/He space (the region inside the dewar, but outside the vacuum chamber) is then sealed off and is pumped down close to the triple point of N_2, to about 100 torr. This lowers the temperature of the collected liquid N_2 further down to 63.5 K. After the apparatus has cooled to this temperature, we follow the normal boil-off and He transfer procedure described in [1].

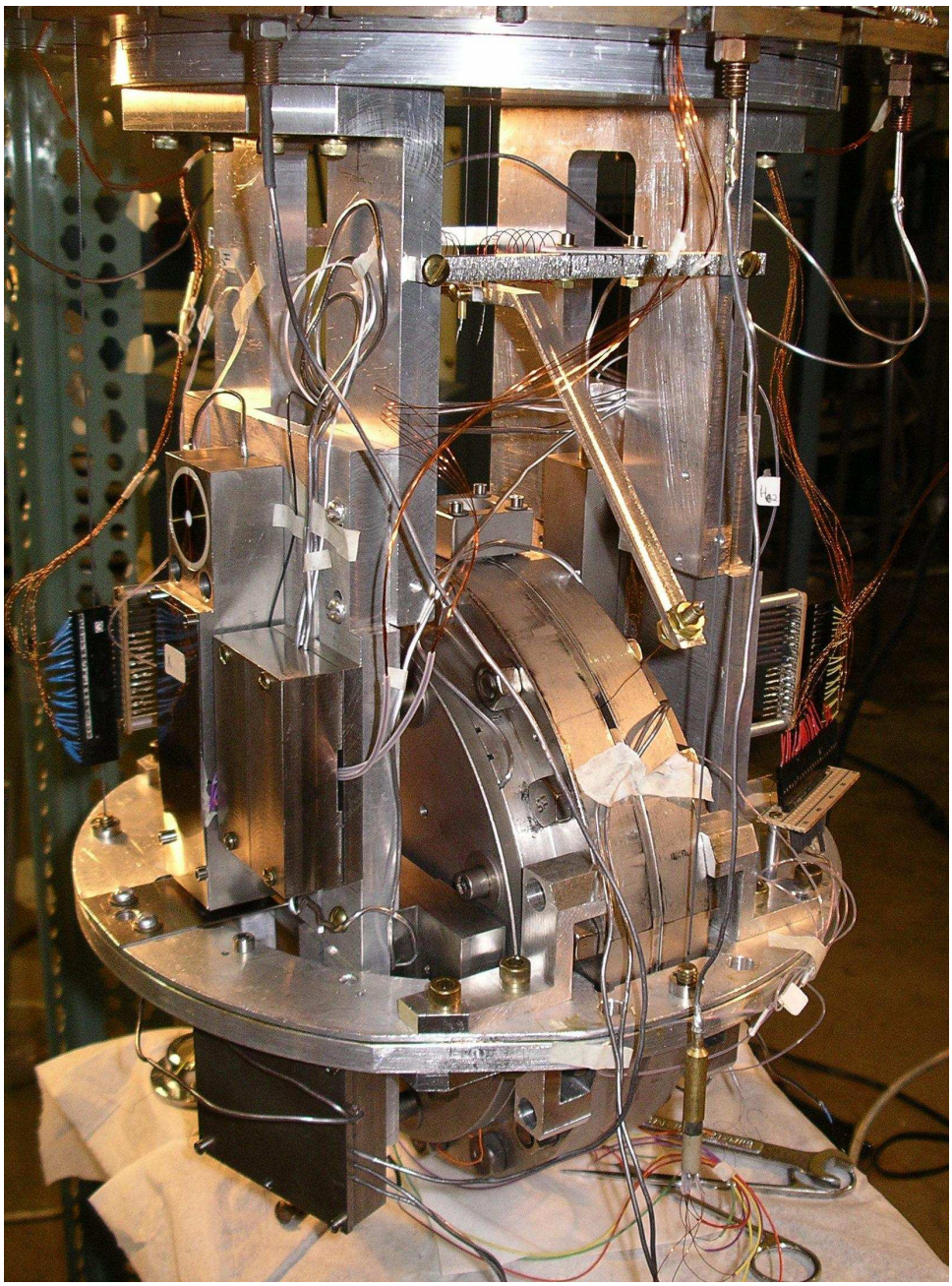

Figure 3.1: Assembled experimental apparatus before cool-down.

3.2 Inductance measurements

The inductance of superconducting coils enclosed in a superconducting cavity is directly proportional to the volume covered by the magnetic field (due to the Meissner effect). As explained earlier, this principle is used to measure the position of the test masses. Thus, an initial measurement of inductances of all the relevant coils provides information about the various initial spacings.

The procedure for inductance measurement is described in detail in [1]. As shown in Fig. 2.9(a), to store a persistent current in a loop, it is connected to a pair of current storing leads (the pair of wires around H_{D2}). The part of the loop between the current leads is wound around a small resistor and is glued to it for good thermal connection. In the steady state, a current sent through the current storing leads will pass through the shorter section of the loop (through the less inductive path). Sending a short voltage pulse to the heat-switch H_{D2} causes that part of the superconducting loop to become normal. The current passing through the current leads is then diverted into the larger section of the loop. As the heat is conducted away and the loop becomes entirely superconducting again, the magnetic flux flowing through the loop becomes trapped in it through the Meissner effect.

The magnetic flux trapped in the loop is a function of the total inductance in the loop and the persistent current that was stored in it. To measure it, the heat-switch is pulsed again, which causes the short section of the loop to become normal and thus develop a small but non-zero resistance. The persistent current then decays over this section and thus a voltage appears across the resistor, which

Circuit	Inductance (μH)
CM sensing coil L_{C1}	12.4 ± 0.2
CM sensing coil L_{C2}	12.5 ± 0.2
CM transformer primary	60.0 ± 0.3
CM transformer secondary	5.5 ± 0.3
DM sensing coil L_{D1}	12.9 ± 0.3
DM sensing coil L_{D2}	13.0 ± 0.3
DM transformer primary	61.4 ± 0.4
DM transformer secondary	5.6 ± 0.4

Table 3.1: Inductances of the sensing circuit coils.

can be measured. It can very easily be shown that

$$\int V(t)\ dt = LI = \phi\ . \tag{3.1}$$

Thus, knowing the current stored in the loop, we can find the net inductance of the loop. By measuring various combinations of the inductors (such as series and parallel), we can estimate the individual inductances.

The inductances of the various coils derived from the measurements are shown in Table 3.1.

3.3 Laser tilt meter calibration

With the procedure described in Section 2.2.7, we were able to measure the laser x-y output sensitivity. The sensitivity, defined as the ratio of detector tilt (in rad) to output voltage, was measured to be $f_{tilt} = 1.57 \times 10^{-4}$ rad/V.

3.4 Sensing circuit transfer function measurements

The transfer function is defined as the the ratio of the output voltage (from the SQUID controller) to the current in the primary of the transformer in the sensing circuit. Essentially, it is a measure of the sensitivity of the sensing circuit and the SQUID.

It is measured by turning on the heat-switch H_{D1} (see Fig. 2.9), and sending a small current through the corresponding current storing leads. The heat used to turn it on must be kept at minimum to prevent excessive spread of heat, which can disrupt the operation of the SQUID. The output voltage is recorded as a function of the input current. The slope of the plot gives the transfer function. The transfer function for the two circuits were measured to be $H_{CM} = 8.71 \times 10^5$ V/A and $H_{DM} = 8.69 \times 10^5$ V/A, respectively.

3.5 Differential accelerometer model

A mathematical model was developed to estimate the CM and DM calibration of the differential accelerometer with the full sensing currents stored in them. The model was mainly developed by Moody [30] and Prieto [17]. In the model, the test

masses are coupled to each other through the sensing currents. The model predicts the current that flows into the SQUID input leads for a given displacement of the test mass.

The key feature of the differential accelerometer model is the characterization of the inductance of the superconducting coil as a first-order function of the position of the test mass x as follows:

$$L(x) = \mu_0 n^2 A \frac{D(d_0 + x)}{(D + d_0 + x)}, \tag{3.2}$$

and the first derivative as

$$\frac{dL(x)}{dx} = \mu_0 n^2 A \frac{D^2}{(D + d_0 + x)^2}. \tag{3.3}$$

Here d_0 is the initial position of the coil with respect to the front superconducting plane (test mass surface), D is the distance to the back plane, n is the turns density for the coil, and A is the area of the coil. For simplicity, we ignore the higher-order derivatives.

In essence, this describes how the magnetic flux trapped in the coil acts as a nonlinear spring linking the test mass to the coil. Several parameters of the coil, such as initial spacing, transformer coupling, and nonlinearity of the inductors can be inferred from the inductance measurements, the transfer function measurements, CM calibration, and measuring the frequency of the test mass fundamental modes as a function of the current (Fig. 3.2).

Figure 3.2 shows the predicted and measured resonance frequencies of the test masses. The measured frequencies are in excellent agreement with the values predicted from the differential accelerometer model that we developed. This shows

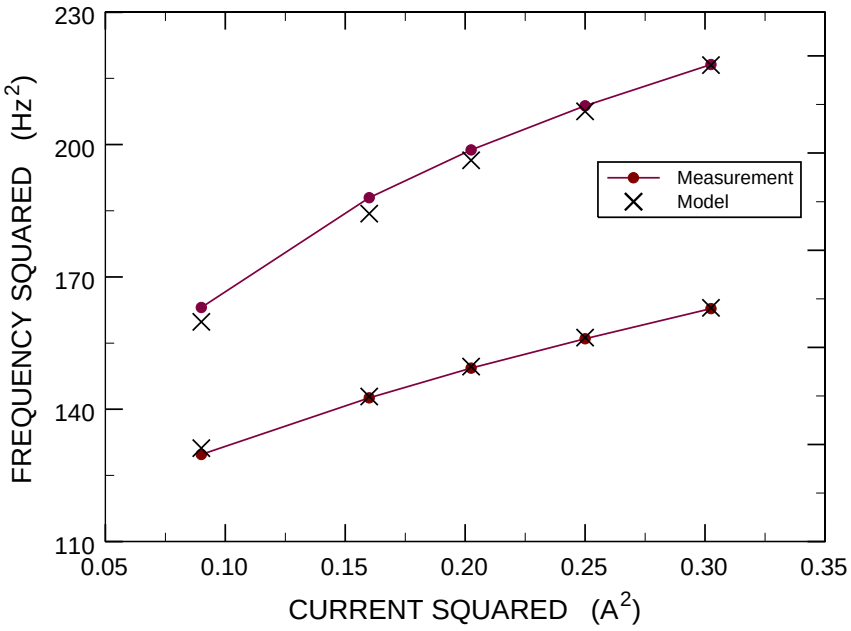

Figure 3.2: Test mass resonance frequencies as a function of the stored series current in the DM circuit.

that our accelerometer model is quite accurate, and we used this model to predict the DM sensitivity.

3.6 Common-mode balance

As described in Section 3.5, our aim is to store the necessary currents in the DM circuit in order to make it *sensitive* to differential motion of the test masses and *insensitive* to CM motion. This is done by driving the housing in CM and adjusting the currents in the DM circuit to reduce the CM response as much as possible. A straightforward and convenient way to apply a CM acceleration to the test masses is

to use earth's gravity by tilting the detector with respect to the vertical. We apply a sinusoidal signal to two of the voice-coil actuators as described in Section 2.2.2. This applies a periodic tilt signal on the detector, and the acceleration produced is simply given by $g\theta$, where θ is the tilt angle.

We initially start with a current of 0 A in *series* and 1.2 A in *parallel* in the DM circuit. We then store a current of 80 mA in the CM circuit. The detector is then driven sinusoidally at a frequency of 0.95 Hz, and we record the CM and DM SQUID outputs and the drive and laser outputs. The CM and DM peak heights and phase difference at the drive frequency are then noted. We then change the currents in the DM circuit (by changing the *series* current by, say, 10 mA) and record the change in the peak heights and phase difference. If the ratio of CM to DM peak heights increases and the phase difference tends towards 90°, then the currents stored were in the right direction (else, we change the direction of the *series* current) and we iterate the process. Eventually, we were able to achieve a balance of better than 10^4 using this procedure.

However, this balance exists only along the sensitive axis (x axis). In practice, the DM output was dominated by the CM and angular acceleration noise from other degrees of freedom.

3.7 Source position and amplitude readout

The source position and amplitude are critical parameters in trying to determine non-Newtonian forces on the test masses or the housing.

Two capacitor plates on opposite sides of the source are connected to form a Wheatstone-type capacitor bridge. As the source mass moves, the bridge output is recorded and fit to the prediction of a two-parameter model, with the source amplitude x_S and offset from the center x_0 as unknowns. The capacitor bridge readout is described in detail in Appendix C.

3.8 CM and DM output calibration

To calibrate the CM output, we need to apply a controlled common acceleration to both the test masses along the sensitive axis. This is done using tilt as described in Section 3.6. We can then use the calibrated laser tilt meter signal to measure the tilt produced. For small tilts, we use the very simple relation $a_c = g\theta$ to calculate the CM acceleration produced. The tilt signal was applied for a period of 2000 s and the measured CM acceleration signal was found to be 0.128 V. With the laser tilt readout already calibrated, as described in Section 3.3, the corresponding tilt produced was $\theta = 9.91 \times 10^{-7}$ rad.

Thus, the CM calibration factor was calculated to be

$$f_{CM} = 7.60 \times 10^{-4} \text{ m s}^{-2}/\text{V}. \tag{3.4}$$

The DM can be calibrated using the CM calibration and the differential accelerometer model. Entering the stored currents in the model, the predicted DM calibration factor was found to be

$$f_{DM} = 1.44 \times 10^{-5} \text{ m s}^{-2}/\text{V}. \tag{3.5}$$

3.9 Baseline measurement

The *baseline* of the differential accelerometer is the distance between the centers of the two test masses. The measurement of the baseline through the procedure described below is the only direct way of measuring the source to test mass separation and a way of confirming the source amplitude. As the source to test mass separation determines the Yukawa force, the baseline is critical in identifying this parameter.

The direct measurement of the baseline is quite challenging. There are two ways of applying a differential force on the test masses. One way is through centrifugal force. If the housing is rotated about the horizontal y axis or the vertical z axis, it produces a centrifugal force on the test masses, which pushes them apart. By knowing the angular velocity provided to the housing (measured through the laser outputs), and the baseline or separation of the test masses, the differential acceleration produced on the test masses by centrifugal force is [1]

$$a_d = l\Omega^2 - l(\vec{\Omega} \cdot \hat{n})^2, \tag{3.6}$$

where $\vec{\Omega} = \Omega\hat{\alpha}$ is the angular velocity about the axis of rotation $\hat{\alpha}$ and $\hat{n}$ is the unit vector along the mean baseline axis. The problem with this method is that it requires large angular velocities to produce sufficiently large centrifugal accelerations and this can create other problems due to nonlinearity.

The other, more reliable, method is to apply a gravitational gradient signal on the test masses at a fixed frequency. To do this, we mounted two large lead (Pb) brick stacks ($\sim$ 36 kg each) on a turntable, as shown in Fig. 3.3. As the bricks move

closer to the dewar, they apply a larger gravitational force on the closer test mass as compared to the other test mass, which produces a differential acceleration signal at the second harmonic of the turntable frequency. By measuring all the distances, we can estimate what the gravitational acceleration signal should be.

As the rotation frequency of the turntable was not constant, we used signal averaging technique to measure the second harmonic acceleration signal. The circuit shown in the figure is used to record the rotation frequency of the turntable, which is used as trigger for the signal averaging.

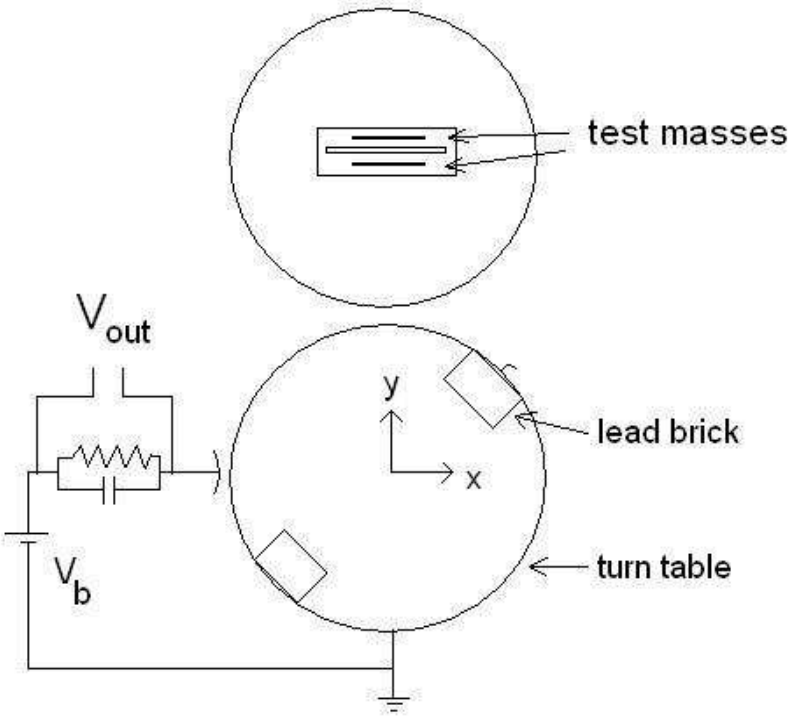

Figure 3.3: Setup for generating a gravity gradient signal and measuring the baseline of the accelerometer.

Assume a Cartesian coordinate system centered on the center of the turntable. The distance to the center of the bricks is R_t. Assuming uniform circular motion and that the bricks start at $(R_t, 0)$, the location of the bricks is given by $x_{b1} = R_t \cos \omega_t t$ and $y_{b1} = R_t \sin \omega_t t$. The position of the other brick is at $x_{b2} = -x_{b1}$ and $y_{b2} = -y_{b1}$.

Assuming all the masses to be point particles, the acceleration of the closer test mass (subscript l) along the y axis can be expressed as

$$a_l(t) = \frac{GM_b(y_{b1} + \frac{b_l}{2} - L)}{[x_{b1}^2 + (L - y_{b1} - \frac{b_l}{2})^2]^{3/2}} + \frac{GM_b(y_{b2} + \frac{b_l}{2} - L)}{[x_{b2}^2 + (L - y_{b2} - \frac{b_l}{2})^2]^{3/2}}, \tag{3.7}$$

and the acceleration of the other test mass (subscript u) becomes

$$a_u(t) = \frac{GM_b(y_{b1} - \frac{b_l}{2} - L)}{[x_{b1}^2 + (L - y_{b1} + \frac{b_l}{2})^2]^{3/2}} + \frac{GM_b(y_{b2} - \frac{b_l}{2} - L)}{[x_{b2}^2 + (L - y_{b2} + \frac{b_l}{2})^2]^{3/2}}, \tag{3.8}$$

where L is the distance between the centers of the turntable and the accelerometer. The differential acceleration can be obtained by differencing Eqs. (3.7) and (3.8).

To measure the signal in the DM output, we first filter the square root of the power spectrum using a band-pass filter limited to about 50 mHz around the second harmonic of the turntable frequency. As the turntable frequency is not very stable, we then use a signal averaging routine to obtain the second-harmonic acceleration amplitude from the filtered signal.

In our experiment, we had $M_b = 35.7$ kg, $R_t = 0.2$ m, $\omega_t/2\pi = 0.108$ Hz, and $L = 0.647$ m. The measured differential acceleration signal (using the CM calibration and the differential accelerometer model) was found to be $a_d = 6.29 \times 10^{-11}$ m s^{-2} rms. Thus, the baseline was found to be 3710 ± 40 μm.

3.10 Post-warmup measurements

After the experiment was warmed up and disassembled, we measured the distances of the capacitor plates and the shields from the rim. Knowing the thickness of the spacer (250-μm thick Nb foil), we can then derive the mean distance between the source mass and the capacitor plates and that between the source mass and the shields. This is useful in estimating the actual source amplitude. While the capacitance bridge measurement yields the modulation of the total gap accurately, it is inaccurate in the estimate of the absolute distance due to large stray capacitance from the leads.

The mean capacitor plate to source distance was found to be 200 ± 14 μm and the mean shield to source distance (d_T) was 210 ± 14 μm.

We can also use this measurement to estimate the baseline. By comparing this to the baseline measured during the experiment, this acts as a check to ensure that the relative distances are not significantly changed when the experiment is cooled to 4.2 K.

The thickness of the source mass was $x_s = 2888 \pm 4$ μm. The thickness of the shields was $x_{sh} = 25 \pm 4$ μm. The thickness of one test mass was $x_t = 240 \pm 4$ μm. The mean distance between the surface of the test mass to the shield surface is more uncertain. From the measured data, we can estimate that the misalignment between the test masses was less than 1/500 rad. Thus, estimating the average misalignment between the shield and a test mass to be $\approx 1/1000 \pm 1/3000$ rad, and knowing the radius of the test mass to be 35.46 ± 0.04 mm, we can estimate that the mean surface

to surface distance between the shield and the test mass was $x_{sht} = 36 \pm 12$ μm.

Therefore, the baseline was $b_l = d_T + x_s + 2x_{sh} + x_t + 2x_{sht} = 3690 \pm 29$ μm. This agrees well with the measured baseline from the previous section. Using the average of these two measurements, the mean surface to surface distance between the source mass and the test mass was thus found to be 280 ± 25 μm.

Though these measurements were made after the experiment was warmed up and disassembled, they were important to confirm the baseline and establish the absolute source amplitude. This was necessary for the data analysis described in the next chapter.

Chapter 4

Data Acquisition and Analysis

In this chapter, I will describe the procedure for data acquisition and the data analysis that was followed for the experiment. Broadly speaking, we performed three experiments and collected three sets of data. The procedure and analysis for each were different so I will describe them separately. The various calibrations and measurements, described in the previous chapter, apply to all of them.

After the cool-down, it was soon apparent that we faced two important error mechanisms. First, there appeared to be a large cross-talk between the source mass and the sensing circuits. This was proved by nulling the stored sensing currents and removing residual sensitivity of the circuits and then driving the source mass. Despite the circuits being insensitive to motion of the test masses, we saw a large signal associated with the source motion. We refer to this as the *magnetic cross-talk error*. Second, we discovered a large coupling between the source mass and the detector housing, which resulted in a large CM signal as the source moved. This is labeled as the *electrostatic force error*.

The procedure for the successive experiments emerged as we gained a better understanding of the error mechanisms and developed ways to try and overcome them. In the first experiment, we tried to study the differential acceleration signal

as a function of the source position. In the second experiment, we tried to cancel the two main errors using techniques discussed later. Finally, in the third experiment, using ideas from the second, we performed an improved version of the first experiment.

The error analysis for all three experiments is summarized at the end. We estimate the various sources of error and compare it to the measured result and error.

4.1 Experiment I: Initial approach

In some of the earlier cool-downs, when the pressure in the chamber had been high, the quality factor (Q) of the source mode was on the order of ~ 1000. We were then able to maintain a stable source amplitude by simply driving the source at fixed frequency and current. With the reduced pressure and improved suspension, the source Q was found to be $\sim 1.5 \times 10^4$. During the initial phase, we found it rather difficult to maintain a steady source amplitude because the Q and the frequency were found to be amplitude-dependent. Since the Q was so high, the drive frequency had to be very precise and we needed to track the frequency change. Eventually, we came up with a very simple control loop to maintain the source amplitude between two specified limits by tracking the source motion.

Once we were able to maintain the source amplitude nearly constant, another issue became apparent. Earlier, we had used the getter to change the pressure inside the chamber, to damp out the motion of the source mass and the test masses. How-

ever, this leads to a significant change in temperature of the source and the detector causing the relative positions and the orientations to change. When the getter is turned off and the pressure drops, the temperature slowly rises to an equilibrium value, thus creating a slow rearrangement of the source and detector. Typically, the time constant in such a process was found to be ~ 3000 s. Once we discovered this, we were able to minimize the getter 'on' time and take into account this thermal rearrangement issue.

4.1.1 Data acquisition

After the above mentioned issues were understood, and some careful measurements were made, it became apparent that the *electrostatic force error* was highly dependent on the source position. It was found in fact to change phase at a certain source position. The DM signal appeared to follow the CM signal. Thus, we decided to measure the error signal as a function of the source position and to keep the source amplitude as similar as possible.

During this initial phase, the random noise floors in the CM and DM outputs were still rather high, as seen in Fig. 4.1. Thus we needed an overnight measurement in order to resolve the signals well enough. Data was then collected for 22 nights.

Figure 4.1 shows the CM and DM amplitude spectrum obtained from an overnight data set of 2×10^4 s. Three suspension peaks of the detector housing are clearly visible in both outputs at 0.41, 0.56, and 0.86 Hz. The fundamental mode ($1f_s$) and the second ($2f_s$) and third harmonics ($3f_s$) of the source motion are

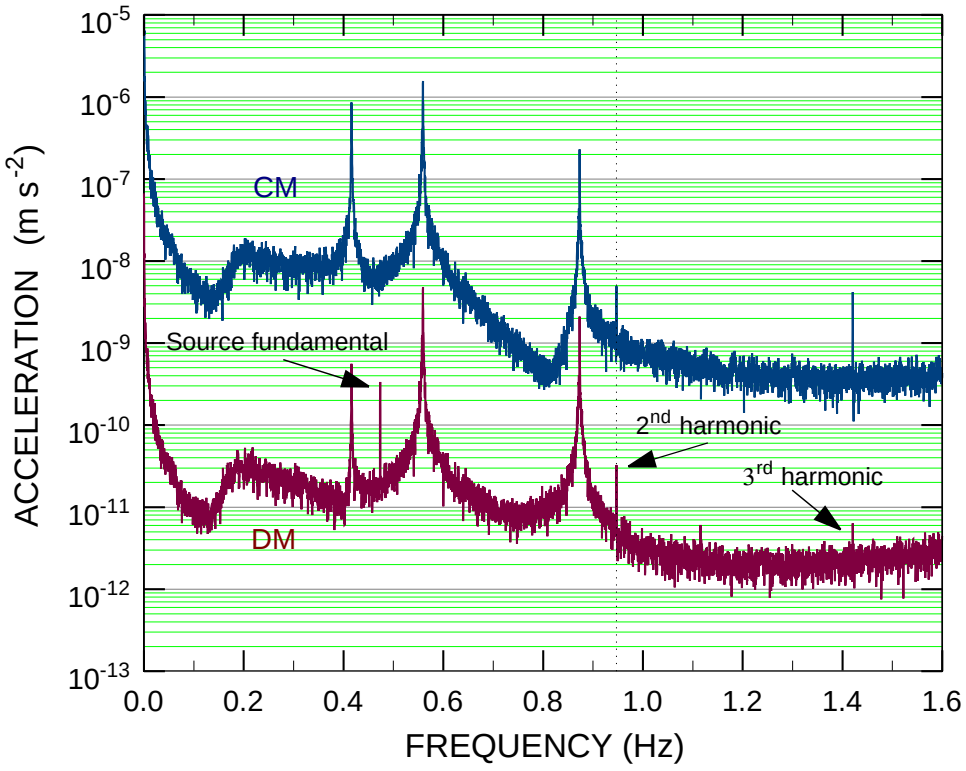

Figure 4.1: CM and DM amplitude spectra for the first experiment.

also visible at 0.473, 0.946, and 1.42 Hz, respectively.

4.1.2 Data analysis

From the strong correlation between CM and DM outputs, it was clear that most of the second-harmonic DM signal at the source frequency was coming from unbalanced CM. Even after removing the CM signal from the DM (residual balance), there was a very clear offset, which could be cross-talk or potentially a Yukawa signal. Therefore, we tried to measure the cross-talk directly, as shown in Fig. 4.2, to try

and subtract it from the DM signal. However, this was rather difficult to do in practice because, without the sensing currents in the DM circuit, the test masses were in a different position, which could affect the amount of magnetic flux (from the source mass) coupling to the sensing circuit. Furthermore, it was difficult to cancel the residual flux in the circuit accurately in order to measure the cross-talk alone. Thus, the cross-talk measured with the currents readjusted, after the above data was recorded, proved to have large errors. Despite these problems, it is possible to do a straightforward analysis of the data shown above to obtain limits on the Yukawa signal in the data.

The source amplitude was measured with the help of the capacitor bridge, as discussed in Section C.2. As the source amplitude was different for each measurement, we normalize the measurements to the mean of the source amplitudes measured, which was 77 μm. This was done by multiplying the CM and DM signals by the ratio of the mean amplitude to actual amplitude for the fundamental, the square of the ratio for the second harmonic, and the cube of the amplitude ratio for the third harmonic.

The cross-talk error, which was measured separately, is shown in Fig. 4.2 as a function of the source position. Assuming a straight-line fit, the cross-talk can be expressed as

$$a_{ct}(x_s) = mx_s + C, \tag{4.1}$$

where m is the slope and C is the intercept of the straight line fit.

Fitting to the data shown in Fig. 4.2, we get $m = 3.86 \times 10^{-7}$ s^{-2} and

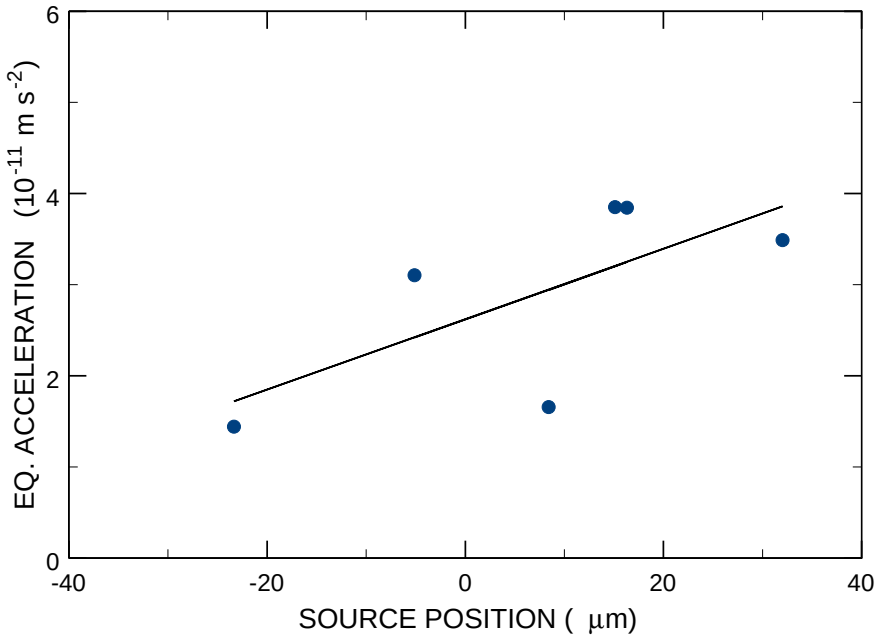

Figure 4.2: Magnetic cross-talk measured at $2f_s$ by the DM circuit as a function of the source position.

$C = 2.62 \times 10^{-11}$ m s^{-2}. The uncertainty in the measurement of the cross-talk is $\pm 7.2 \times 10^{-12}$ m s^{-2} for each point. Note that this is a systematic error and needs to be subtracted from the DM data. The uncertainties, being uncorrelated, add as the square root of the sum of their squares. Subtracting this straight line from the DM data removes the magnetic cross-talk from it. We can then plot the DM and the CM outputs as functions of the source position, as shown in Fig. 4.3. As seen from the plot, the CM and DM accelerations at $2f_s$ are highly correlated indicating that they both have the same origin.

For comparison, we also compute and show the acceleration signal we would

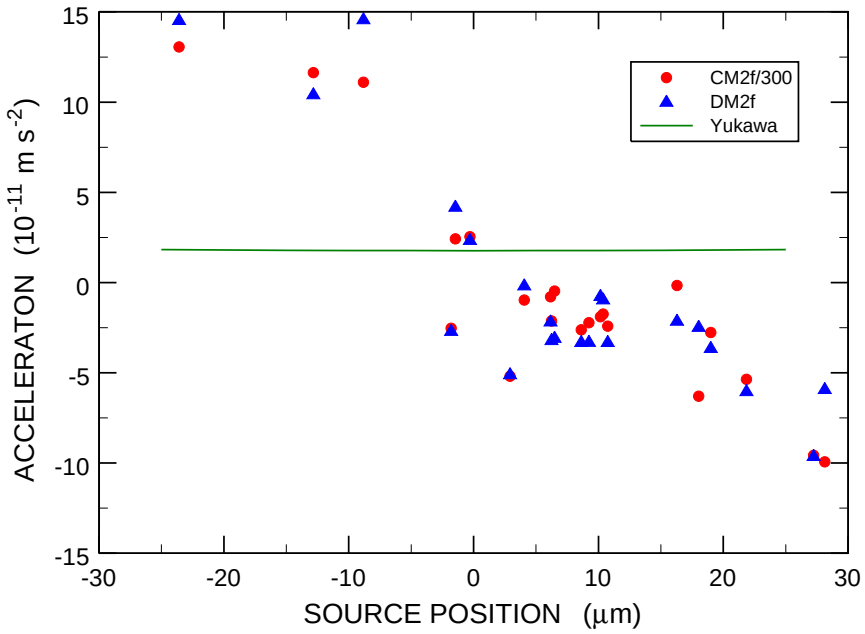

Figure 4.3: CM and DM outputs as a function of source position.

expect to see in the DM output for a Yukawa-type potential with $\alpha = 10$ and $\lambda = 100$ μm. It is important to note here that a Yukawa potential would generate a CM signal, only if the source mass was not symmetrically located with respect to the test masses. Even then, the CM acceleration produced by a Yukawa potential with $\alpha = 10$ and $\lambda = 100$ μm would be two orders of magnitude smaller than the typical CM noise floor for an overnight measurement. Henceforth, we can safely conclude that the CM acceleration signal is produced by non-Yukawa sources.

For further clarity, we can plot the DM outputs versus the CM outputs as shown in Fig. 4.4. As the Yukawa potential would generate very little CM signal, it would appear simply as a horizontal line in such a plot. Assuming the CM

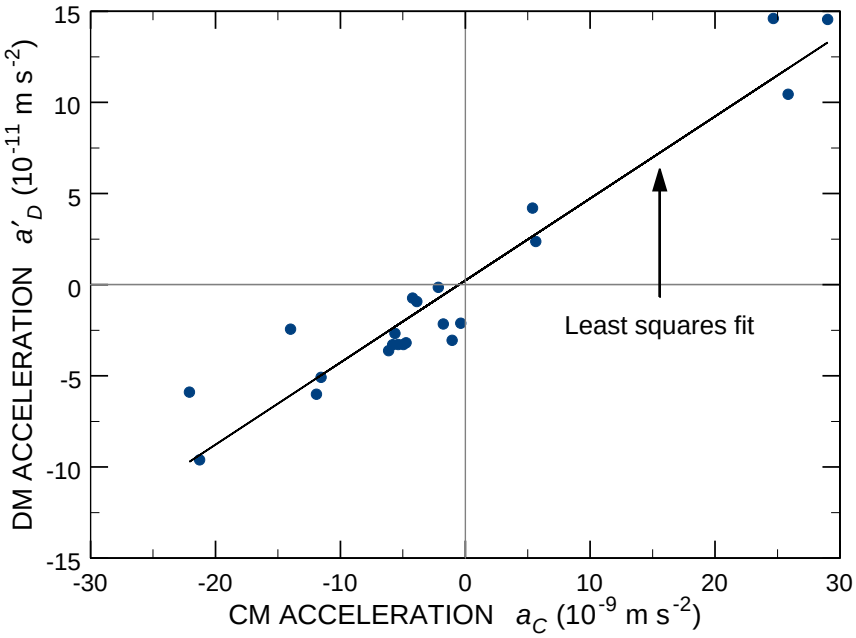

Figure 4.4: Plot of DM output as a function of the CM output.

rejection remains constant throughout this data set, we can remove the unbalanced CM error by fitting this data to a straight line. This is equivalent to a *residual balance* described by Moody, Paik and Canavan [22]. However, the measurement error for each point differs significantly because the seismic noise in the CM and DM outputs were different each night. Therefore, we use the scheme of weighted total least squares regression [31, 32, 33] to obtain a straight line (see Appendix D) expressed as

$$a'_D = \Delta h_C \; a_C + a_D, \tag{4.2}$$

where Δh_C represents the residual CM sensitivity of the differential accelerometer and a_D is the true differential acceleration. The result is $a_D = (4.9 \pm 8.2) \times 10^{-12}$

m s^{-2}.

The error due to the electrostatic coupling is reduced by this method because the DM accelerations were proportional to the CM. However, the overall error in a_D is increased by this procedure as compared to a'_D, because of the addition of the random noise in the CM measurement. This is because the direction of the sensitive axis and the direction of the DM acceleration error produced by this coupling were different.

It is interesting to observe the cross-talk error at the fundamental shown in Fig. 4.5. Note that the $1f_s$ cross-talk is about ten times larger, but more uniform and shows less dependence on source position compared to the $2f_s$ cross-talk. This would suggest that the source position dependence in Fig. 4.2 is mostly due to residual flux in the circuit.

Some of the main drawbacks of the above approach were:

1. Small source amplitude.

   We were only able to achieve a mean source amplitude of 77 μm out of the total gap of 200 μm. The chief reason for this was that we we were trying to vary the source position, which resulted in the amplitudes being smaller at the extreme positions. Also, we had not yet optimized the source-detector orientation. The sensitivity to deviations increases rapidly as the source mass approaches the test mass. Thus, being much further away from the expected amplitude for the source mass reduced the sensitivity considerably.

2. Inaccurate cross-talk measurement.

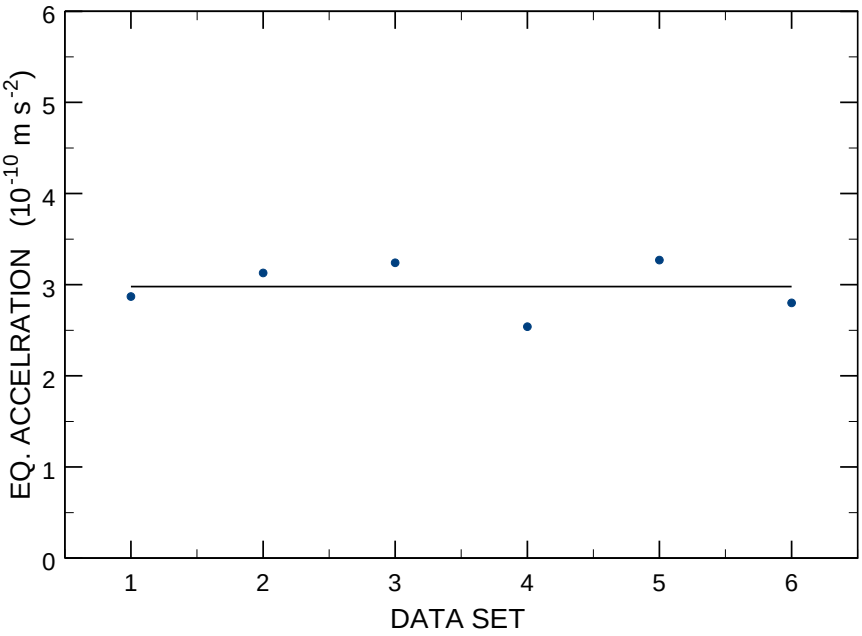

Figure 4.5: Cross-talk measured by the DM circuit at $1f_s$.

The cross-talk measurement in the above data set had rather large scatter, as shown in Fig. 4.2, and thus increased the error in the DM considerably.

3. Large error terms in CM output.

   The second-harmonic error terms in the CM, and consequently the DM outputs, were rather large in comparison to their respective noise floors. Trying to remove large DM signals increases the error in the final result due to increased random errors.

Due to these drawbacks, we then tried a different approach to try and overcome the above difficulties.

4.2 Cross-talk cancellation

Soon after recording the initial set of data, we discovered a very simple and elegant method to remove the cross-talk more reliably from our DM channel. In the DM output, the direction (phase) of motion of the test masses sensed by the sensing circuit depends on the direction of the currents stored in the circuit, whereas the magnetic cross-talk should be independent of the current stored. Thus, to remove the cross-talk, we needed to simply *reverse* the direction of all the sensing currents stored and *subtract* the two outputs to eliminate the cross-talk. If the two outputs are summed instead, the acceleration signals are canceled and the cross-talk signals are added. Thus we can simultaneously measure the cross-talk along with the signal and reliably separate the two.

We do make some assumptions in using the above method. This approach assumes that the cross-talk remains constant for the two measurements. This had been found to be true for the data shown earlier and was also justified in the data taken later. However, there were indications that the cross-talk varied over much longer periods of time. It was also affected by increasing the temperature of the entire housing and source mass to above the superconducting transition temperature of Nb and cooling it slowly back to 4.2 K. In spite of this slow variation of the cross-talk, this cancellation method is superior to the earlier method of measuring and subtracting the cross-talk. The error in the measurement of cross-talk increases the overall error in the DM outputs significantly when it is subtracted from the DM outputs. With this new method, we circumvent this problem entirely by simply

combining two measurements with reversed currents.

There is some error associated with this method, due to the fact that not all quantities other than the cross-talk were duplicated precisely in the second measurement. For instance, the sensing currents might be slightly different, or the vertical orientation of the detector might be different, both of which might affect the balance. Furthermore, there were some large swings in the temperature of the lab during some of the measurements. Even though the temperature of the vacuum chamber is maintained constant at the temperature of the liquid He bath, the lab temperature seems to affect the room-temperature components of the suspension, such as the rubber tubes in the detector suspension, etc., which affects the detector tilt. Again, this results in a change in the CM balance.

A change in the CM balance amounts to a change in slope of the DM versus CM plot. However, since these errors are random by nature, they will appear as part of the statistical error in the DM versus CM plot and do not need to be accounted for separately. Still, we can make a crude estimate of the cross-talk error by assuming that the change in balance from one data set to the next is less than 1%.

In the measurements described henceforth, the cross-talk error has been removed by the procedure described above. The measured cross-talk is shown in Appendix B.

4.3 Experiment II: DC voltage bias method

Rather than try and measure the large CM signal and try to remove it from the DM output, we considered the possibility of removing the CM signal in the second harmonic. We came up with the idea of applying a DC bias voltage to the capacitor plates, which would create additional coupling between the source mass and the housing. As this coupling would be nonlinear, we could generate a force with a $2f_s$ component and, by applying this voltage to only one side of the capacitor plates, we could control its sign. This additional signal could be used to cancel out the CM signal at $2f_s$. We refer to this as 'error compensation'.

However, as we had discovered from the previous measurement (Fig. 4.3), the CM $2f_s$ error was highly sensitive to the source position. It was hard to recover and maintain the exact same source position for each overnight data set. Therefore, we chose to set the source position at a location that would maximize its amplitude within reasonable limits. Based on the typical drifts and ability to position the source, we set a limit of ± 10 μm on the source position. This meant that the CM $2f_s$ signal would vary up to $\pm 3 \times 10^{-8}$ m s^{-2}. Thus, the bias voltage was different for each data set.

4.3.1 Data acquisition

The procedure for this measurement was as follows:

1. Store the appropriate alignment currents in order to position the source with respect to the detector at a fixed distance within reasonable limits ($\sim \pm 10$

μm). These values were chosen so as to keep the source close to the center and parallel with respect to the capacitor plates.

2. Store the sensing currents in the sensing circuits.

3. Drive the source to an 88-μm amplitude and measure the $2f_s$ signal in the CM output (typically for a period of 3000 s).

4. Apply a DC bias voltage to one of the capacitor plates to try and cancel the measured $2f_s$ signal in the CM output. Record the data overnight for a period of 40000 to 50000 s.

5. The sensing currents were then reversed every alternate day and the procedure was repeated.

Figure 4.6 shows an example of how the second-harmonic error term was reduced by using a voltage bias.

4.3.2 Data analysis

The data analysis was very similar to Section 4.1.2, but there were some differences, such as the way the cross-talk was removed. For each data set, we pick a 40000-s section that has stable source amplitude, no DM and CM SQUID overloads, and the lowest noise floor in the CM power spectrum.

After selecting this section, we compute the source amplitude, as described in Section C.2. Just as before, we compute the square root of the power spectrum of the CM and DM outputs. We then record the values of the signal amplitude and

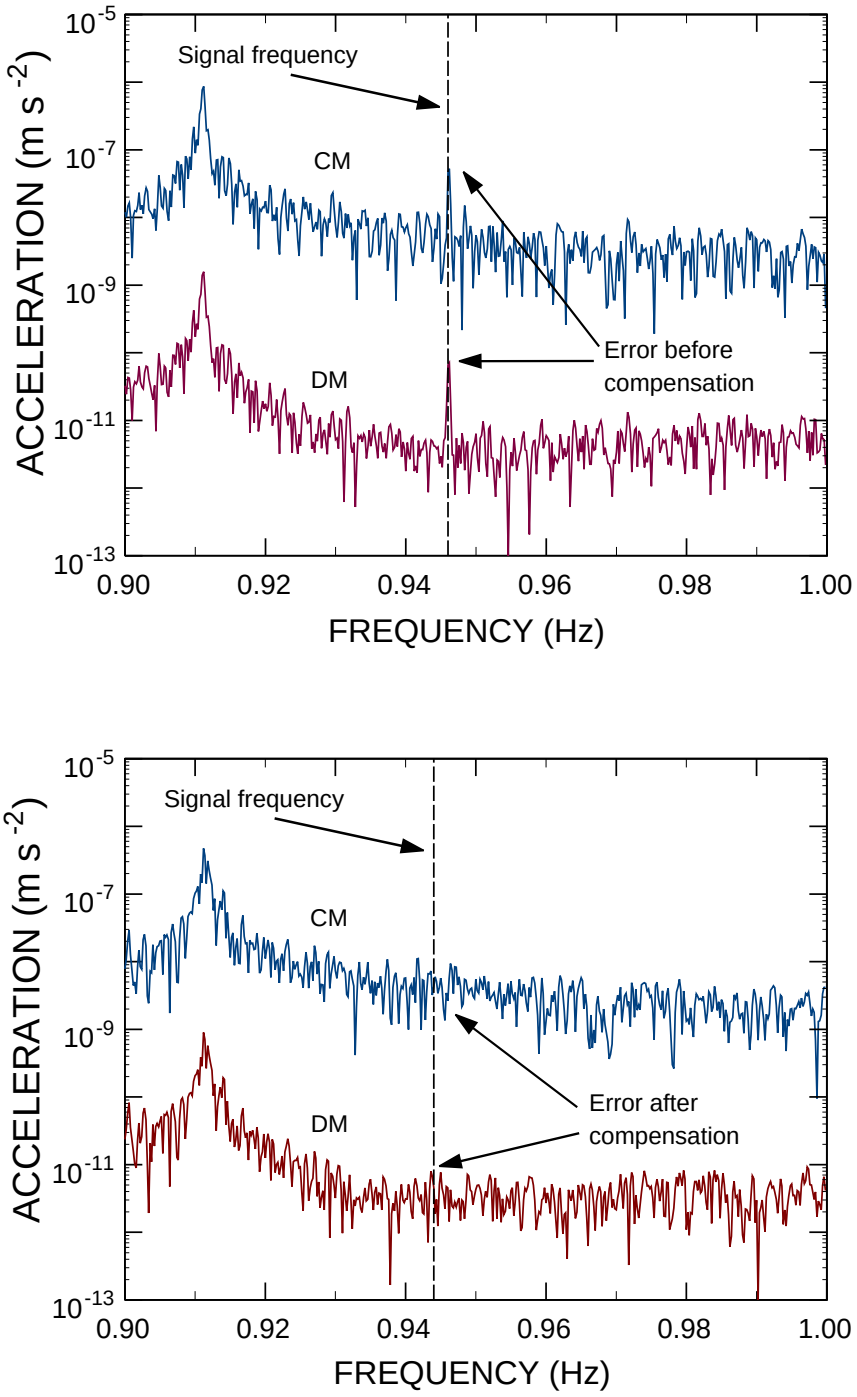

Figure 4.6: Frequency response of the outputs of the sensing circuits before and after error compensation.

phase at the source $1f_s$, $2f_s$, and $3f_s$ frequencies in the spectrum. The phase of the signals is computed with respect to the source motion (the fundamental).

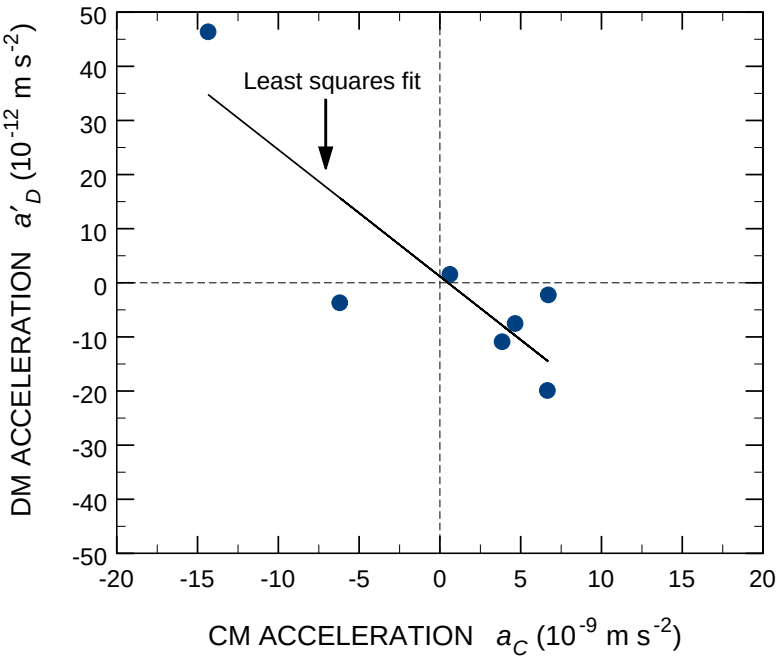

Figure 4.7: Residual DM signal as a function of the residual CM signal and a least squares straight-line fit.

The signal amplitudes in the CM and DM spectra are then normalized to a standard source amplitude (we used 88 μm, which is the mean amplitude for the entire set). Then, we subtract all the amplitudes from two data sets taken on consecutive nights with currents reversed and divide by two. This procedure allowed us to cancel the cross-talk while preserving any real motion-based signal.

The data collected from 14 nights is shown in Fig. 4.7. Again the data shown can be used to plot a straight-line fit, and we can estimate the error and the intercept

of the fit. As before, we measure the noise floors of the CM and DM channels near the $2f_s$ frequency and use them to do a weighted total least squares regression. The result is $a'_D = (1.2 \pm 3.8) \times 10^{-12}$ m s^{-2}.

The main limitations of this experiment were:

1. Poor cancellation.

   While the CM $2f_s$ cancellation appeared to work well over short periods, we found a significant drift in the $2f_s$ peak during an overnight measurement. Thus the cancellation was often poor.

2. Increased angular acceleration error.

   We also realized later that applying this bias voltage on the capacitor plates was increasing the effective coupling between the source and the detector and could result in a larger angular acceleration error. This mechanism is described in detail in Section 4.5.

4.4 Experiment III: Final set

During the above data set, we noticed that the torsional mode of the housing was very close to the $2f_s$ frequency of the source. Thus, the torsional resonance peak was increasing the seismic noise in the CM and DM backgrounds considerably (especially so in CM, since the mode was not pure rotation about the z axis, but seemed to also contain significant amount of tilt as well). As discussed after Eq. 4.2, due to residual balance, the random error in a_D is a combination of the error

in DM and CM $2f_s$ measurements. It would therefore be very desirable to shift the torsional resonance peak away from 0.95 Hz to reduce the random error.

The natural torsional mode of the housing was close to 0.73 Hz when it was initially cooled down. As discussed earlier, alignment currents were necessary to free the source mass. But storing the alignment currents (in particular, the current which rotates the housing about z) increased the frequency up to 0.91 Hz. By adjusting the dewar tilt and adjusting the source suspension very carefully, we were able to reduce the alignment currents required to free the source mass. Consequently, the torsional mode frequency was lowered to about 0.82 Hz. This resulted in a significant improvement in the CM noise levels near the $2f_s$ frequency. The improvement was marginal in the DM noise floor.

We were also able to adjust the detector suspension in such a way as to slightly increase the source amplitude. Thus an amplitude of 97 μm was achieved.

4.4.1 Data acquisition

The procedure for this experiment was the following:

1. Store the appropriate alignment currents in order to position the source with respect to the detector at a fixed distance within reasonable limits ($\sim \pm 10$ μm). Here the objective was to maximize the amplitude of the source.

2. Store the sensing currents in the sensing circuits.

3. Drive the source to a 97-μm amplitude and record the data overnight for a period of 30000 to 50000 s.

4. The sensing currents were then reversed every alternate day and the procedure was repeated. In between reversing the currents, we measured cross-talk with no currents stored in either circuit. This was indicative of the cross-talk with the test masses pushed out.

Figure 4.8 shows the acceleration spectral density of the CM and DM outputs measured overnight for a period of 40000 s.

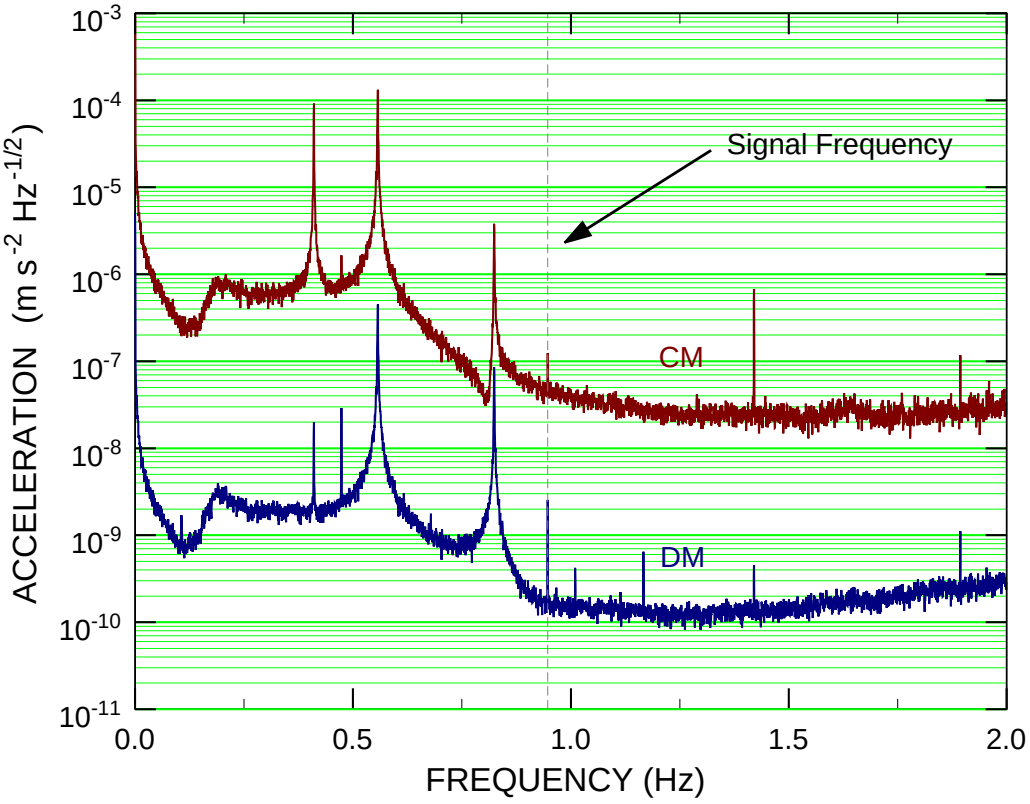

Figure 4.8: CM and DM amplitude spectra for the third experiment.

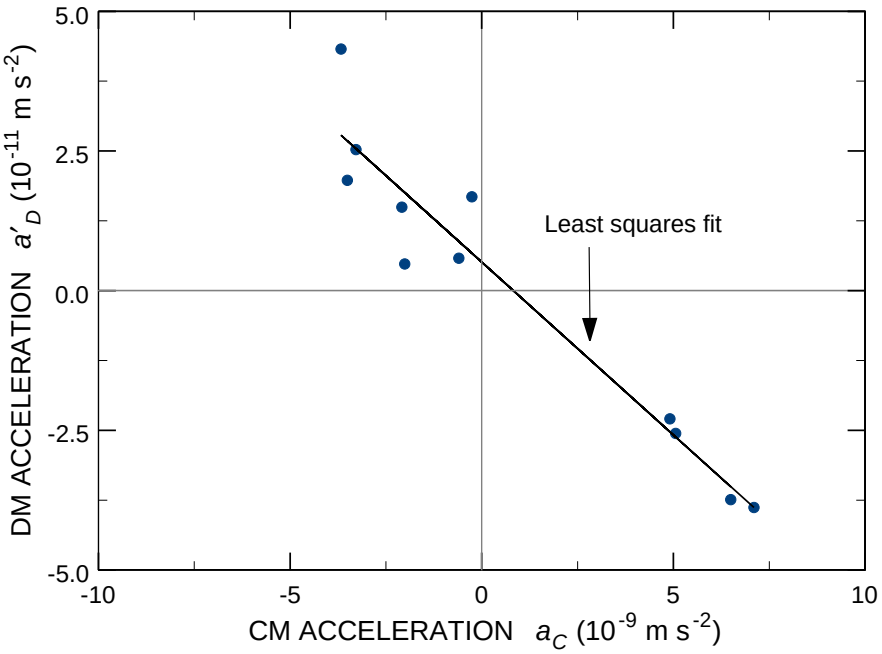

Figure 4.9: Residual DM signal as a function of the residual CM signal at $2f_s$ and a least squares straight-line fit.

4.4.2 Data analysis

For data analysis, we followed a procedure identical to Section 4.3.2. After eliminating the cross-talk by subtracting neighboring sets of data with the currents reversed, we can plot the DM output as a function of the CM outputs, as shown in Fig. 4.9.

Figure 4.9 shows the $2f_s$ data. Assuming a straight-line fit (again, using weighted total least squares regression), we get the residual DM acceleration signal at $2f_s$ to be $a'_D = (5.3 \pm 2.2) \times 10^{-12}$ m s^{-2}.

While the above result appears to imply a violation signal, we noticed that the

data was somewhat inconsistent within sections. The initial part of the data showed a positive violation signal while the latter half showed a negative violation signal. This led us to believe that the excess DM signal could be due to angular motion of the housing induced by the strong source-detector coupling. In the next section, we discuss a model to explain this angular motion and show that the excess DM acceleration measured above could in fact be coming from the angular motion of the housing. This would then imply that the angular motion could create a systematic error in the experiment.

4.5 Electrostatic force model

Electrostatic coupling between the source mass and the detector housing causes both linear and angular acceleration of the housing. Linear acceleration is rejected through CM balance. However, angular acceleration produces DM through asymmetries in the system. In addition, the electrostatic coupling deflects the shields due to their finite rigidity. This in turn produces CM and DM acceleration on the test masses due to a similar force from the shields.

We considered a very simple model to understand and explain the signals in the CM and DM outputs and their dependence on various parameters. The detector housing is a large heavy and complex structure, which can be approximated as two connected disks with a small gap between them. To simplify the analysis, we will assume that it has simple linear pendulum modes at 0.41 Hz along the y axis and at 0.55 Hz along the x axis. However, there is clear evidence that the torsional mode

axis is significantly offset from the z axis. This is taken into account in the form of an offset parameter δL, which represents the distance by which the torsional axis is offset from the z axis.

The source is modeled as a disk, which is free to have any alignment with respect to the detector housing and assume any position within the gap. When the source is centered within the gap, the distance between the source surface to the surface of the housings is d_g.

Consider a patch-effect type interaction between the source mass and the housing (see Section 2.4.6). Assuming that the crystal/impurity sizes are much larger than the gap d_g, the force can be expressed as

$$F_p(d) = -\frac{1}{2}\frac{\epsilon_0 V_p^2 A_s}{2d_g^2}, \tag{4.3}$$

where V_p is an average potential difference between the detector housings and the source mass, A_s is the area of the source mass, and d_g is the separation between them when the source is perfectly aligned and centered.

The source position and orientation within the gap can be characterized by three quantities: the source-center offset x_0, the source inclination about the y axis θ_y, and the source inclination about the z axis θ_z. The frequency of the rotational mode of the detector about the y axis is about five times higher than that about the z axis. Since the torques on the detector about y and about z are expected to be similar, the angular acceleration about y would be much smaller than that about z. Therefore, we neglect the source inclination about the y axis.

Now, let the source undergo linear oscillation with an amplitude a_s. Consider

a thin vertical strip of the source mass located at a displacement x from the center and thickness δx. The distance of this strip from the sides of the housing gap can be expressed as

$$d'_g = d_g - x_0 - x\theta_z - a_s \cos\omega_s t. \tag{4.4}$$

Ignoring edge effects, the infinitesimal force between a small part of the source mass and one side of the housing can be expressed as

$$\delta F_p(t) = -\frac{1}{2}\frac{\epsilon_0 V_p^2 \sqrt{2(R_s^2 - x_s^2)}\delta x}{2{d'_g}^2}. \tag{4.5}$$

The net force can then be expressed as

$$F_p(t) = \int_{-R_s}^{R_s} \delta F_p(t). \tag{4.6}$$

The net torque about z axis + δL is

$$\tau_p(t) = \int_{-R_s}^{R_s} \delta F_p(t)\ (x + \delta L). \tag{4.7}$$

Rather than solve these equations analytically, the force and torque values were numerically computed for various configurations of the source and detector as a function of time. Based on the time signals, we computed the amplitude spectra for the linear and angular accelerations. The value of V_p was determined by fitting the fundamental of the CM output of the model to the measured value. Using the measured data for the third experiment, we found $V_p = 0.27$ V. This number is comparable to CPD measured in other experiments [28].

From the model, it appears that the source-center offset x_0 is chiefly responsible for the $2f_s$ CM output. The CM $2f_s$ term changes sign as x_0 changes sign and an

estimated value of $x_0 = 5$ μm gives $a_C = 3 \times 10^{-9}$ m s^{-2} at $2f_s$, which is close to the mean of the absolute value of CM $2f_s$ terms from the data. The mean of x_0 over the entire set is ~ 0 μm since the mean of the CM $2f_s$ terms is close to zero.

The test mass misalignment δl can be estimated with the help of the capacitor bridge. Note that the capacitor bridge output measures the relative motion between the source mass and the detector. As the motion at the torsional mode frequency (f_τ) of the detector is coming from the detector itself and not the source, we can difference the output of the two horizontally located capacitors to measure the angular acceleration of the detector at f_τ. The CM output should not be sensitive to this angular acceleration at f_τ but the DM will be sensitive to it due to δl. Comparing the angular acceleration to the DM output and using Eq. (2.3), we estimate the misalignment to be $\delta l \approx 250$ μm.

Both δL and θ_z contribute in creating angular motion of the detector due to source motion. However, the effect of δL depends upon x_0. Thus, the angular acceleration produced due to δL leads to the proportionality between the CM and DM accelerations. The residual balance removes the error introduced by this term.

A finite value of θ_z, say, about 10^{-4} rad, leads to a nearly constant angular acceleration term for small variations of x_0. Once again, the capacitor bridge can be used to measure the orientation of the source with respect to the capacitor plates. Based on the fact that the alignment, used in experiment III, gave us the best orientation between the source and the detector housing, and using the capacitor bridge measurements, we estimate the orientation of the source with respect to the detector as $\theta_z = (0 \ \pm \ 3.7) \times 10^{-5}$ rad.

Using the above parameters, we were able to calculate the residual differential acceleration due to angular motion of the detector housing to be $a'_D = (0 \pm 2.5) \times 10^{-12}$ m s^{-2}. This would imply that we have an additional systematic error equal to a'_D in the third experiment. Indeed, a similar error exists in the other two experiments as well and can be estimated similarly. For experiment I and II, this error is $(1.4 \pm 1.2) \times 10^{-12}$ and $(6.4 \pm 2.5) \times 10^{-12}$ m s^{-2}, respectively.

The shields were modeled as a spring-mass system. We were to unable to measure the shield frequency in our experiment. In [1], where 12.5-μm Nb foil was used for the shield, their frequencies were measured to be ~ 1 kHz. Since we used a 25-μm thick foil for the shields, we expect their frequencies to be ~ 2 kHz. Using the electrostatic force model from above, we can estimate the force applied by the source mass on the shields and calculate their displacement. Using similar force magnitudes between the shields and the test masses, we compute the $2f_s$ DM acceleration to be 1.1×10^{-13} m s^{-2}. Since we do not know the actual magnitude and sign of this acceleration, we consider the computed value as an error.

Taking the additional systematic errors from the angular motion and shield deflection into account, the final results in the three experiments become

$$a'_D = (3.5 \pm 8.3) \times 10^{-12} \text{ m s}^{-2}, \tag{4.8}$$

$$a'_D = (-5.2 \pm 4.6) \times 10^{-12} \text{ m s}^{-2}, \tag{4.9}$$

$$a'_D = (5.3 \pm 3.3) \times 10^{-12} \text{ m s}^{-2}. \tag{4.10}$$

With this rather simple model, we were able to infer some general principles:

1. If the source were perfectly centered without any offset or misalignment, then the net force on the detector would have only odd harmonics. There would be no angular motion produced and thus the DM output would simply have the unbalanced CM.

2. Even harmonic components, including a second-harmonic term, can be produced in the CM and the DM outputs from two causes − a source-center offset and a source-detector misalignment. A pure source-center offset produces even harmonic terms in the CM, which will produce a proportional term in the DM due to misbalance. On the other hand, source-detector misalignment can produce angular motion in the detector, which can produce even harmonic terms in the DM through test mass misalignment, as discussed in Section 2.4.3.

3. If the detector rotation axis does not pass through the center, then this creates additional angular motion, which can appear as a signal in the DM.

The real situation could be much more complex. The capacitor plates may not be lined up uniformly with the shield. The angular motion of the detector could be more complicated. The actual distribution of the voltages could vary over the surfaces. The above model provides a potential explanation for the excess DM output seen in the experiment and also identifies an error mechanism, angular acceleration of the detector housing, which could hinder further improvement without additional instrumentation.

4.6 Measured experimental errors

In this section, we will describe the important experimental errors measured. This is useful as a check to ensure that the errors displayed in the data were close to the sum of all the experimental errors. This ensures that we have accounted for all the errors in the experiment correctly.

4.6.1 Intrinsic noise

Figure 4.10 shows the amplifier and thermal noise of our sensing circuit and SQUID. It is measured by recording the SQUID voltage output with zero sensing current and using the DM calibration factor discussed in Chapter 3. From the graph, the amplifier noise near the $2f_s$ peak of source mass is $\sim 1 \times 10^{-11}$ m s^{-2} Hz$^{-1/2}$, which is very close to the theoretical prediction described in Section 2.4.2.

4.6.2 Total random noise

This section discusses the measured total random noise, which includes the intrinsic noise, seismic noise, and other random noise present in an overnight measurement, such as due to drifts in the source and detector position and orientation.

As explained previously, the seismic noise couples into the DM channel through misalignment. Therefore, if the CM balance along the sensitive axis were to be better than the misalignment, then the noise floor in the DM would be limited by the seismic noise from the other degrees of freedom. This indeed seemed to be the case in our experiment.

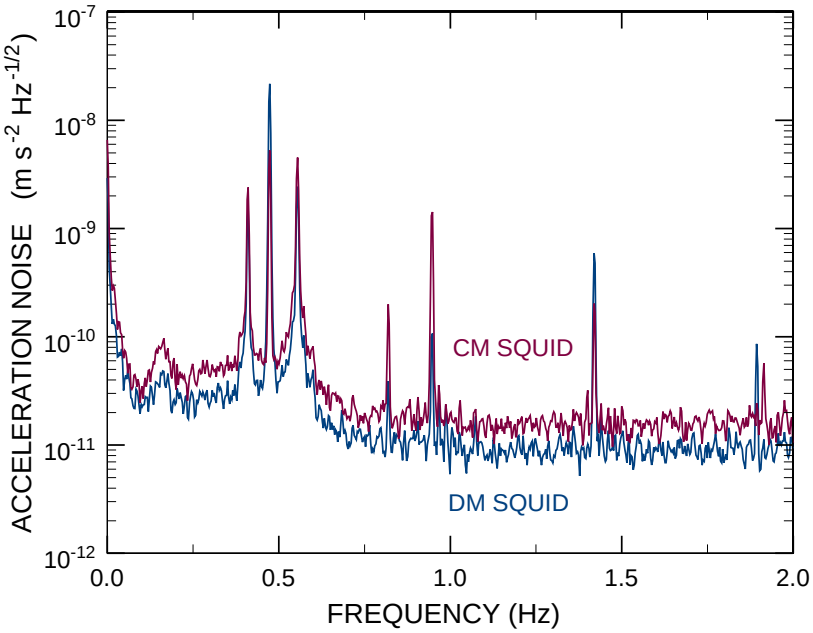

Figure 4.10: Acceleration noise spectral density of the two SQUID sensors.

Due to the large source-detector interaction force (which we chiefly attribute to electrostatic forces), there was a large CM motion created in the housing, which appeared in the DM output through imperfect balance. We were then able to use the measured CM output to subtract this interaction from the DM output (known as residual balance). While this did reduce the overall error in the DM output, it added noise from the CM channel into the DM. Thus we must take into account the error (chiefly seismic) in the CM channel as well.

The seismic noise is measured as the square root of the mean of the power spectral density in a small bandwidth on either side of the $2f_s$ frequency. The sum of the residual CM noise and the DM noise gives the total seismic noise in

the three experiments, which were 5.7×10^{-12}, 4.9×10^{-12}, and 2.6×10^{-12} m s^{-2}, respectively. The total seismic noise accounts for most of the random noise in any single measurement.

The total random noise listed in the table above is about 20 times greater than the seismic noise listed in Table 2.1 for the following reasons: As explained above, the random noise in the final result included seismic noise from both CM and DM channels. Furthermore, there was additional random noise due to drifts in the source and detector position and orientation.

4.6.3 Cross-talk error

The cross-talk error was one of the most important error sources in all the experiments. They are plotted and described in detail in Appendix B.

Being a systematic error source, the cross-talk error depends upon the source amplitude. The cross-talk error in the different experiments are 7.2×10^{-12}, 6.1×10^{-13}, and 5.1×10^{-13} m s^{-2}, respectively.

4.6.4 Electrostatic force error

The electrostatic coupling between the source mass and detector resulted in both linear and angular motion of the detector. Using the CM output, we were able to reject the linear motion of the housing to the level of the CM noise. However, since there was no way to measure the angular motion of the detector, we were unable to remove this effect from the DM data. A simple model allowed us to place

limits on the angular acceleration produced from such a coupling and allowed us to calculate the additional systematic noise due to this.

This error varies with the source amplitude. The electrostatic force error in the three experiments are 1.2×10^{-12}, 2.5×10^{-12}, and 2.5×10^{-12} m s^{-2}, respectively.

4.6.5 Summary of errors

The various experimental errors are shown in Table 4.1. The metrology error was computed from the measured source surface variation. The total error agrees well with the errors displayed in the data.

As seen from the table, experiment III had the best noise floor. Yet, it was larger than the intrinsic noise limit of the detector by a factor of ~ 300. Thus, we need to reduce the electrostatic coupling error and the seismic noise significantly in order to reach the ultimate sensitivity of the detector.

4.7 Experimental result

The measured differential acceleration of the test masses due to the source motion at the second-harmonic frequency for the three experiments are

$$a'_D = (3.5 \ \pm \ 8.3) \times 10^{-12} \text{ m s}^{-2}, \tag{4.11}$$

$$a'_D = (-5.2 \ \pm \ 4.6) \times 10^{-12} \text{ m s}^{-2}, \tag{4.12}$$

$$a'_D = (5.3 \ \pm \ 3.3) \times 10^{-12} \text{ m s}^{-2}, \tag{4.13}$$

for source amplitudes of $\delta d = 77,\ 88,$ and 97 μm, respectively.

Error source	Exp. I ($\times 10^{-13}\,\mathrm{m/s^2}$)	Exp. II ($\times 10^{-13}\,\mathrm{m/s^2}$)	Exp. III ($\times 10^{-13}\,\mathrm{m/s^2}$)
Metrology	0.01	0.01	0.01
Total random noise	57	49	26
Magnetic cross-talk	72	6	5
Electrostatic coupling	12	25	25
Total	93	55	36

Table 4.1: Total measured error for source to test mass spacing of 281 μm, and source amplitudes of $\delta d = 77,\ 88,$ and 97 μm.

We can use Eq. (1.1) to compute the limit on α for a given λ. The source and test masses are modeled as parallel disks and the Yukawa force is integrated over the respective volumes as a function of the distance. As mentioned earlier, for symmetric distribution of the masses, the real-time Yukawa signal has only even harmonic components. We then associate the above results with a Yukawa force, which gives us

$$\alpha = 2.0 \pm 4.7, \tag{4.14}$$

$$\alpha = -2.2 \pm 2.0, \tag{4.15}$$

$$\alpha = 1.9 \pm 1.2 \tag{4.16}$$

at $\lambda = 100$ μm.

Taken together, the weighted mean can be expressed as

$$\alpha = 0.9 \pm 1.0 \tag{4.17}$$

at $\lambda = 100$ μm. This constitutes a null result. The error represents one standard deviation of the experimental error. Figure 4.11 shows a plot of the current sensitivity (2σ) of the experiment. We also show the resolution goal of an improved experiment being designed currently. This is described in the following chapter.

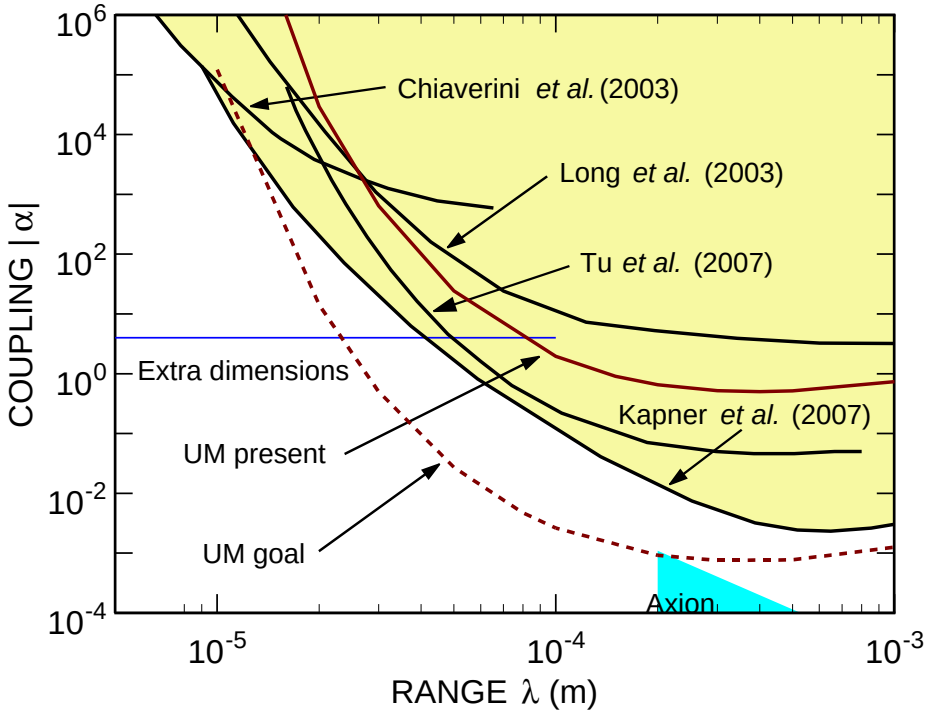

Figure 4.11: The present sensitivity of the University of Maryland experiment (95% confidence) versus the existing limits. Also shown is the goal of our improved experiment.

Chapter 5

Future Improvements and Conclusion

In this chapter, I will present suggestions to improve the experimental result and obtain better limits and I will summarize and present the conclusions of the experiment we performed in Fall 2009 to test the gravitational ISL at sub-millimeter distance scales.

5.1 Limitations of the current experiment

As seen from Section 4.6.5, the current experimental noise is still about 300 times the amplifier noise limit. An electrostatic coupling error, magnetic cross-talk, and seismic noise are the three important sources of error to be overcome before we can achieve the ultimate sensitivity of the experiment.

As the model described at the end of Chapter 3 indicates, there exists an electrostatic coupling between the source mass and the detector. This interaction induces complex motion in the detector, which appears to be both linear and angular. Linear motion (along the sensitive axis) shows up in the DM channel through misbalance, whereas angular motion appears due to misalignment. In addition, the electrostatic coupling produces shield displacement, which in turn produces DM acceleration of the test masses. This may be a significant source of error in future

experiments.

We were sensitive to the linear motion through the CM channel, and were able to successfully remove it in each of the three experiments. However, the excess DM output produced from angular motion can only be modeled currently.

The seismic noise was expected to be the limiting noise source in the experiment. It was found to be larger than expected due to the reasons discussed in Section 4.6.5.

Another source of concern was the drift in positions and orientations of the source and the detector. A large contribution to this was from drift in temperature of the lab. The air-conditioning unit for the lab was malfunctioning through the course of the experiment and the temperature in the lab varied by as much as 10° F. To do a more accurate experiment, it would be best to maintain a better control over the temperature.

5.2 Suggested improvements

We stand to gain the most by trying to reduce the coupling between the source and the detector. A standard procedure for reducing electrostatic forces between parallel plates is applying a voltage bias to cancel the contact potential difference between the plates [27]. Unfortunately, in our experiment, there are multiple surfaces involved − the two shields, the source mass, and the eight capacitor plates. Each of these might have a different contact potential, thus a voltage bias is unlikely to reduce the electrostatic forces significantly. Nevertheless, this procedure can be at-

tempted and might shed some interesting information about the electrostatic forces involved.

To reduce shield displacement, we could further tighten the shields, thereby increasing their stiffness. A shield frequency greater than 5 kHz might be achievable. The shield could also be clamped in the middle, increasing the stiffness drastically.

If the coupling cannot be reduced significantly, then we must either reduce its effect on the detector or measure/model it, and remove it from the data as precisely as possible. One way to reduce the acceleration of the detector housing would be to stiffen the suspension modes by introducing additional springs. Another advantage of introducing these springs is that the linear and angular suspension modes could be made more distinct and their directions could be better controlled. This would have a couple of undesirable consequences:

1. It would reduce the vibration isolation by the square of the ratio of the final to initial suspension frequency, thus the test mass resonance peaks would be higher by that factor. This might force the DM SQUID to be operated at a less sensitive range, thus reducing the sensitivity. Moody [30] pointed out that this problem could be overcome by doing a wide-band balance and by organizing the experiment wiring to minimize parasitic modes.

2. It will also increase the seismic noise level near the $2f_s$ source peak. Of course, with the additional accelerometers installed, this may not be a problem.

3. Additionally, this might make it harder to free the source mass as the alignment currents required to move the housing would have to be larger.

Due to these limitations, we estimate that the suspension modes cannot be stiffened by more than a factor of two, which may not reduce the detector acceleration significantly. It may also worsen the situation by locating some of the housing modes close to the $2f_s$ of the source motion. Thus, stiffening the detector suspension offers some advantages and has some negative consequences, and a more careful examination will have to be made before choosing this course.

As described in Section 2.4.3, the random noise in the experiment was dominated by the seismic noise. It is possible to reduce this noise source below the amplifier noise limit, by measuring the seismic noise in all relevant degrees of freedom and subtracting it. A simple way to do this is to couple additional SQUIDs to the alignment circuits and thus measure the detector motion in four degrees of freedom (two linear degrees, y and z, and two angular degrees, about y and about z). At the same time, we can also measure the source-induced motion of the detector housing, which produces a DM signal in an identical manner as the seismic noise (i.e., through misalignment).

Replacing the Nb source mass with a Ta source mass would also improve the experiment. Being nearly twice as dense as Nb, it would result in a factor of two increase in signal strength. Furthermore, it will be maintained above its superconducting transition temperature, thus it will not trap magnetic flux through it. This could possibly reduce the cross-talk problem significantly.

5.3 Conclusion

We successfully performed an experiment to test for deviations from the gravitational ISL. A Newtonian null source mass, in the form of a disk of large diameter to thickness ratio, was driven between two small disk-shaped test masses. The test masses were coupled via superconducting coils, with persistent currents stored in them, to form a differential accelerometer.

The cold-leaks in the cryostat were fixed and a charcoal-based cryopump was installed in the vacuum chamber to overcome the residual gas pressure error. A capacitor-bridge based source position readout was developed, which worked very well.

In the course of the experiment, we discovered the two dominant sources of error in the experiment: magnetic cross-talk and electrostatic coupling between the source mass and the detector. Both were reduced, using different techniques, to levels comparable to the limiting random noise in the experiment.

Three tests were performed with different source amplitudes and different procedures, which successively reduced the net measurement noise. Expressing the deviation from the ISL as a Yukawa potential, the final result from the experiment was found to be

$$\alpha = 0.9 \pm 1.0 \tag{5.1}$$

at $\lambda = 100$ μm, which is a null result. The error represents one standard deviation of the experimental error.

We are currently also redesigning and improving this experiment by following

the suggestions given in Section 5.2. With this improved experiment, we hope to approach the amplifier noise limit, the UM goal in Fig. 4.11, and be capable of resolving deviations from the ISL at the level of $|\alpha| = 1$ at $\lambda = 28$ μm.

Appendix A

Pressure-mediated coupling

In a cool-down performed in August 2008, we discovered an important residual gas mediated coupling between the source and test masses. As Prieto had pointed out [1], at that time, there was a small leak in the chamber, which required us to pump the chamber continuously in order to maintain low pressure.

The pressure inside the vacuum system is measured at the top of the cryostat by a Philips ion gauge. It is connected to the chamber through a 1-inch diameter tube made out of Fiberglas G-10. The gauge and the Cu tube are at room temperature and the G-10 tube extends from room temperature to 4.2 K.

During the cool-down, after the source mass was freed, sensing currents were stored in the DM and the CM circuit and a balance of 300 was achieved. We then drove the source mass at resonance to an amplitude of 100 μm and looked for a signal in the DM and CM outputs. We found a highly variable signal, which was strongly correlated with the pressure in the vacuum chamber. Figure A.1 shows a plot of the $2f_s$ error terms in the DM channel as a function of the pressure readout from the gauge. The $2f_s$ error terms were normalized for a source amplitude of 100 μm.

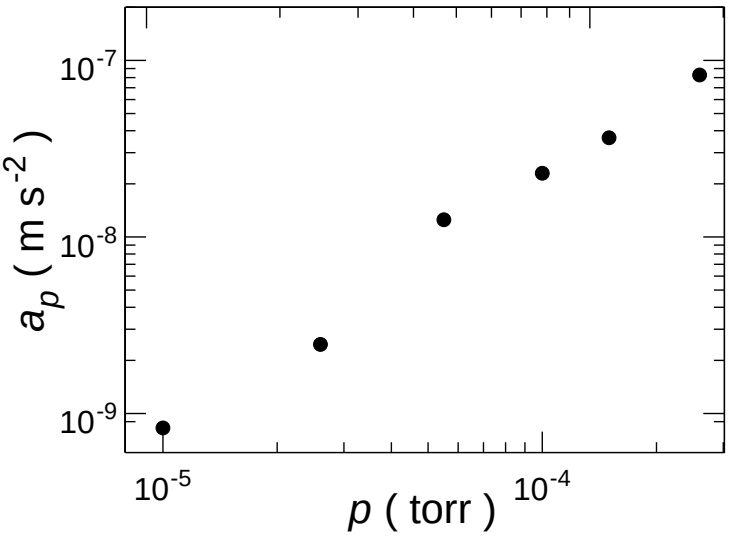

Figure A.1: Acceleration error versus pressure.

From the data, the error term can be best described by

$$a_d(p) = 0.23 \text{ m s}^{-2} \ (p/\text{torr})^{1.7}. \tag{A.1}$$

A.1 Error model

To explain the data shown above, we considered a model where the residual gas pressure couples the source motion to that of the shields, and the pressure once again couples the shields to the test masses.

The mean free path of the He atoms in the vacuum chamber can be calculated as

$$l = \frac{k_B T}{\sqrt{2}\pi d_g^2 p_c} = 13.2 \text{ m}, \tag{A.2}$$

where k_B is the Boltzmann constant, $T = 4.2$ K is the temperature, d_g is the

diameter of the gas molecule, and p_c ($\sim 10^{-5}$ torr) is the pressure in the vacuum chamber. This is much larger than the source to shield gap, which is about 240 μm. Thus, as the source mass moves between the shields, the atoms bounce between the source mass and the shields, and the number of reflections depends on the distance between the two. Thus, as the source moves closer to one side, it exerts a greater force on one shield than on the other. This interaction can be described by the following model.

Assuming that the temperature remains constant, then from Boyle's law, the pressure is inversely proportional to the volume of the gap V. Thus the increased force on the shield due to the source mass motion (change in pressure) can be described as

$$\delta f_{sh} = \frac{p_c A_{Sh} d_g}{d_g - a_s}, \tag{A.3}$$

where A_{Sh} is the area of the shields and a_s is the amplitude of the source mass.

From this, we can estimate the displacement of the shields at the second harmonic to be

$$\delta x_{Sh} = \frac{\delta f_{sh}}{m_{Sh}[(2\omega_s)^2 - \omega_{Sh}^2]}, \tag{A.4}$$

where $m_{Sh} = 1.2$ g is the mass of the shields, $\omega_s/2\pi = 0.473$ Hz is the resonance frequency of the source, and $\omega_{Sh}/2\pi \approx 500$ Hz is the resonance frequency of the shield.

A similar coupling as above should exist between the shields and the test masses. The force on the test mass due to shield displacement can be expressed as

$$\delta f_t = \frac{p_c A_{Sh} x_{sh}}{d_t}, \tag{A.5}$$

where d_t is the distance between the shields and the test mass.

The acceleration would then be given by

$$a_t = \frac{\delta f_t}{m_t[(2\omega_s)^2 - \omega_t^2]}, \tag{A.6}$$

where m_t is the mass of the test mass and $\omega_t/2\pi$ is the resonance frequency of the test mass. Substituting from Eqs. (A.3), (A.4) and (A.5) gives the relation between the residual pressure and the test mass acceleration as

$$a_t \propto p_c^2. \tag{A.7}$$

While this model is a reasonable approximation, it is clearly missing some complexity to fully explain the data. Nevertheless, it explains the chief mechanism by which the residual gas pressure can provide a large coupling between the source and the test mass.

From the data and the model above, the residual gas pressure in the chamber would have to be less than $\sim 5 \times 10^{-8}$ torr in order to keep the test mass acceleration to below 1×10^{-14} m s^{-2}.

A.2 Lowering residual gas pressure

In order to trace the leak, we used a He leak detector (Leybold-Heraeus Ultratest-F). For large leaks ($> 10^{-7}$ torr m^3 s^{-1}), the normal procedure is to evacuate the chamber and then connect it to the spectrometer in the leak detector. When He gas is sprayed outside the region where the leak is located, the spectrometer shows a spike in He level, thus pinpointing the leak. However, this proved ineffective for

our vacuum chamber since the volume of the chamber was rather large compared to the size of the leak, so the leak rate was too small to be detected clearly. Thus, we had to go through a very long and painstaking procedure of carefully taking apart the chamber and testing different sections for the leak. In this way, we were able to identify two components which were leaking − a home-made feedthrough for SQUID leads and a stainless steel bellows. Both of these components were replaced and we found no further leaks in the chamber. When the vacuum chamber alone was subsequently pumped out and cooled to 4.2 K, the pressure gauge read a stable pressure of 1.4×10^{-6} torr.

To lower the pressure further, we then developed a simple charcoal-based adsorption pump (see Fig. A.2) based on [34]. It consists of a rectangular and thin Cu plate (dimensions: $0.15 \times 10 \times 8$ cm). Charcoal flakes are bonded to both surfaces using Eccobond 286 epoxy. The plate can be heated using two 200 Ω power resistors, and the temperature is measured by a carbon resistor glued to the Cu plate. The Cu plate was held by a stainless steel threaded rod which was rigidly fixed to the vacuum can. A pair of high purity Cu wires provided heat-sinking between the plate and the can.

Due to its porous nature, a charcoal flake has a very large surface to volume ratio. When it is cooled to sufficiently low temperatures, it traps a large quantity of gas molecules, which adhere to its surface. It can thus 'pump' most gases very quickly. He gas is the hardest to pump, and it requires a temperature of less than $10-11$ K to pump He effectively. It begins to release the gas above this temperature and releases almost all the trapped He gas above ~ 30 K. Thus the pump is normally

on, once the chamber cools below 11 K and is turned off by heating the getter.

The charcoal getter plate was tested on a separate insert and dewar which had a similar arrangement for measuring the pressure. Despite varying the initial conditions and trying different heat-sinking techniques, we were unable to get pressure significantly lower than 10^{-6} torr. We then learned that controlling the temperature of the top portion of the cryostat (which is at room temperature), where the pressure gauge was connected to, had a significant effect on the pressure readout by the gauge. This implied that the pressure read by the gauge was dominated by outgassing from the room-temperature part of the cryostat insert. The pressure presumably was lower inside the vacuum chamber but it was not clear what it actually was. When the room-temperature part of the insert was cooled to near 273 K, the pressure reading from the gauge dropped to $\sim 2 \times 10^{-7}$ torr, hence it suggested that the actual pressure inside the chamber could be lower than this. Without any direct way to measure the chamber pressure, we thought it best to continue with the experiment cool-down and establish limits on the pressure through other means.

An important consequence of reducing the pressure was a dramatically different equilibrium temperature of the experiment and associated thermal time constant. This was of course because of the drastically reduced residual gas conduction. Based on some of these measurements, we were able to establish an upper limit on the chamber pressure to be $p < 3 \times 10^{-7}$ torr. In some of our initial cool-downs after the leak was fixed, the equilibrium temperature of the detector was found to be as high as ~ 6 K. In order to maintain a much lower detector temperature, we had to heat-sink both the detector and the source mass with Cu braids (cleaned soldering

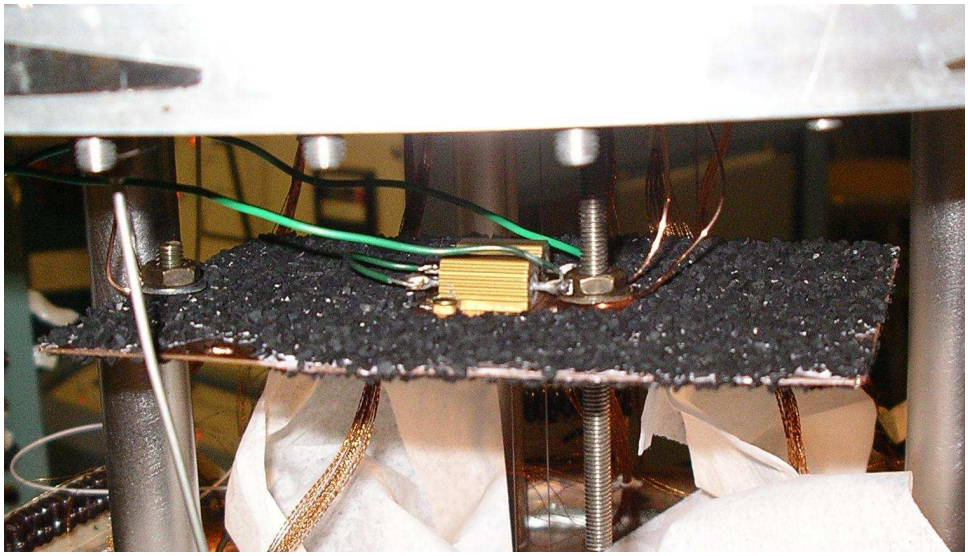

Figure A.2: Charcoal getter.

wicks) and Cu wires, respectively.

Appendix B

Magnetic cross-talk error

After we were able to lower the pressure in the chamber sufficiently, we immediately discovered our next most important error source, namely, magnetic cross-talk. In this section, I will briefly summarize our findings and discuss the causes and the steps taken to reduce each probable cause.

We had made some design modification to the source and detector suspension, as described in Section 2.2.2. The noise floors of the CM and DM spectra were improved significantly due to the lowered suspension frequencies. The source mass was freed by storing currents in the alignment circuit.

The source was then driven up to an amplitude of 80 μm, with no current stored in the sensing circuits. We found a rather large signal in the SQUID outputs at the harmonics of the source frequency. This signal was found to be highly variable but it was not clear what it depended on. Its maximum value was 1 mV, which would correspond roughly to an acceleration of 10^{-9} m s^{-2}.

It therefore appeared that there was some kind of coupling between the source and the SQUIDs that was independent of the sensing currents. We then tested for any cross-talk with the source driving coil, by sending the driving current through a similar coil without driving the source mass. There were no indications of any

cross-talk with the driving current. The other possibility was that the cross-talk was coming from the source itself. The Nb source mass is a superconductor at its equilibrium temperature. Thus it could trap magnetic flux through it as it cooled or it could have magnetic contamination.

There are several ways that such a coupling/cross-talk could exist:

1. Magnetic cross-talk through the sensing circuits.

   The electromagnetic shield between the test mass and the source does not work perfectly. There are gaps present at its sides, which allow some magnetic flux coming from the source to leak into the region where the sensing coils are located, thus there could exist a coupling between them.

2. Direct magnetic cross-talk to the SQUID input coil.

   The SQUID housing was originally designed as two pieces − a housing and a cover. Although the gap between the cover and the housing was very small, magnetic flux from the source could leak into the housing and thus be picked up directly by the SQUID input coil.

3. RF modulation.

   The capacitor plate leads at the top of the cryostat were connected to the capacitor bridge through a rather long and unshielded cable. We found that removing this cable seemed to reduce the cross-talk. One possible mechanism for this could be the following: The long cable might act as an RF antenna and introduce a large RF field in the gap between the source and the detector.

SQUIDs are very sensitive to any RF. As the source moves, it might modulate the RF picked up by the SQUID, which might appear as a signal.

In some of our early cool-downs, we found that the cross-talk was dominated by mechanism 2. This was found by looking for cross-talk with the SQUID heat-switch turned on. This should have reduced the current coming from the sensing circuits dramatically, but it was found not to affect the cross-talk significantly.

As we made improvements to reduce this mechanism of cross-talk, at various times it was found to be dominated by mechanism 1 and possibly by mechanism 3. Thus all three mechanisms were likely active and contributed to the cross-talk.

B.1 Design improvements

We made a number of successive improvements to try and overcome all the above mechanisms:

1. New SQUID housing.

   In our initial cool-down, we discovered that the cross-talk persisted even when the SQUID heat-switch was turned on. In other words, the cross-talk was nearly unaffected when a resistive component was introduced in the sensing circuit. This strongly implied that a significant part of the cross-talk originated from a direct magnetic cross-talk to the SQUID input coil. To test this theory, we tested the SQUID housing separately. A SQUID was placed in it and it was lowered into a He dewar. We then applied an AC magnetic field with the help of a large diameter coil located outside the dewar.

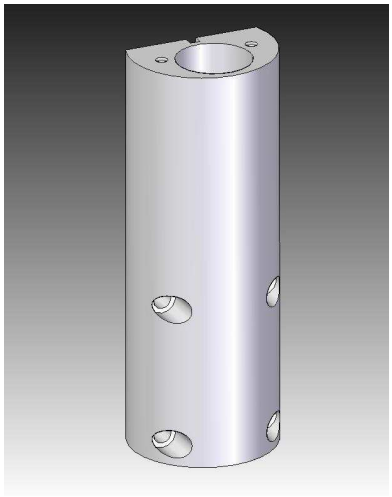

Figure B.1: New SQUID housing.

We found that the housing provided an attenuation on the order of 10^5 to the magnetic field. This was improved by up to two orders of magnitude by using several layers of Pb foil clamped between the cover and the SQUID housing and wrapped around it. However, there was an improvement of nearly five orders of magnitude on using a large length to diameter cylindrical cavity and placing the SQUID inside it. Based on these measurements, we decided to machine a new SQUID housing, as shown in Figure B.1.

2. Improved shielding of the sensing circuits.

   After the SQUID housing was improved and we significantly reduced direct coupling to the SQUID, we found that there was still some cross-talk to the SQUID. This time, it appeared to be reduced when the SQUID heat-switch was turned on, indicating that it was coupling through the sensing circuit. To reduce this coupling, we tried to shield all leads as much as possible by

enclosing them in Pb tubes and using Pb foil to cut off gaps through which flux could leak into the circuits, as shown in Fig. B.2.

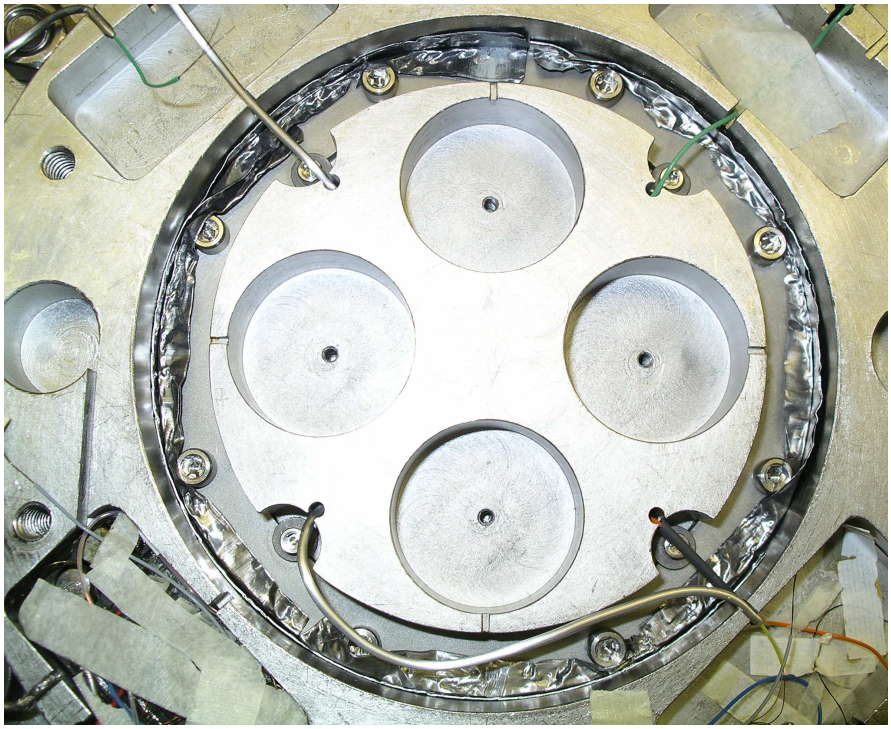

Figure B.2: Using Pb foil to shield the sensing circuits.

3. RF shielding.

   We improved the RF shielding by using a grounded cable for the capacitor leads and using an inductive filter ($\sim$ 10 μH) at the input of the capacitor leads.

With all these modifications in place, we were able to reduce the cross-talk by almost two orders of magnitude. The new Ta source will be operated above its superconducting transition temperature. With no magnetic field trapped we expect

that the cross-talk due to mechanisms 1 and 2 would be significantly reduced but mechanism 3 would still contribute.

B.2 Measured experimental cross-talk

As described in Section 4.2, we were able to cancel the cross-talk by repeating a measurement with all the sensing currents reversed. The two sets of measurements are then added, and we remove the remaining CM dependent term by multiplying it by the slope of the CM versus DM plot and subtracting it. Figures B.3, B.4 and B.5 show plots of the cross-talk at $1f_s$, $2f_s$, and $3f_s$, respectively, for the second experiment (using the voltage bias).

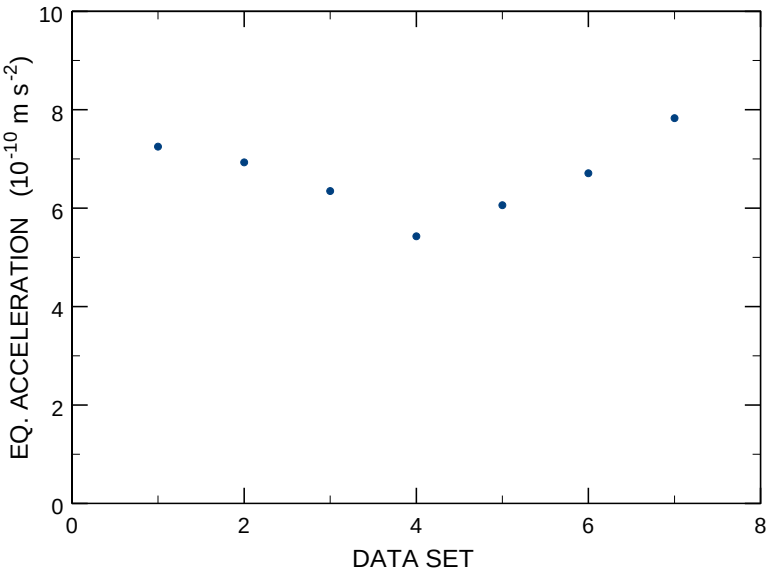

Figure B.3: Exp. II: DM $1f_s$ cross-talk.

From the graphs, it is clear that all the cross-talks seem to have a very similar

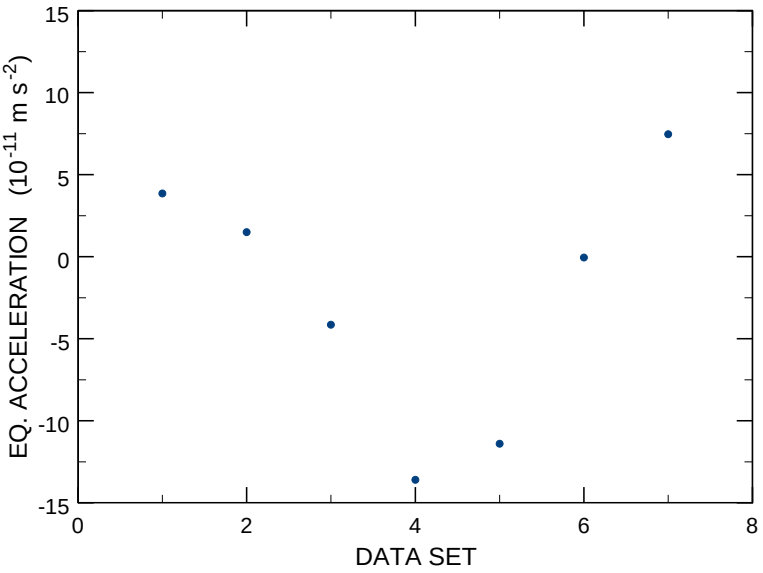

Figure B.4: Exp. II: DM $2f_s$ cross-talk.

trend, especially, the $1f_s$ and $2f_s$. We are not clear on the cause, but removing it improves the data considerably.

In the third experiment, the cross-talks were much more constant throughout the entire set. Figures B.6, B.7, B.8, and B.9 show the cross-talk for the entire set at the $1f_s$, $2f_s$, $3f_s$, and $4f_s$.

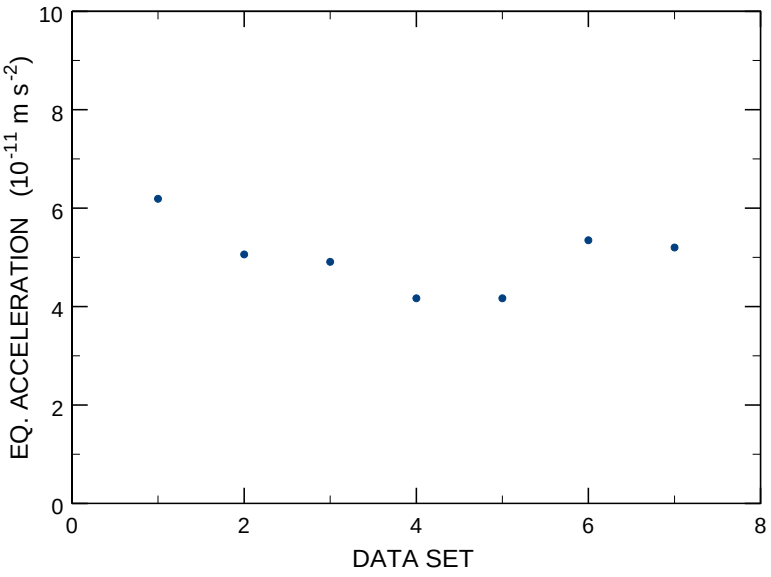

Figure B.5: Exp. II: DM $3f_s$ cross-talk.

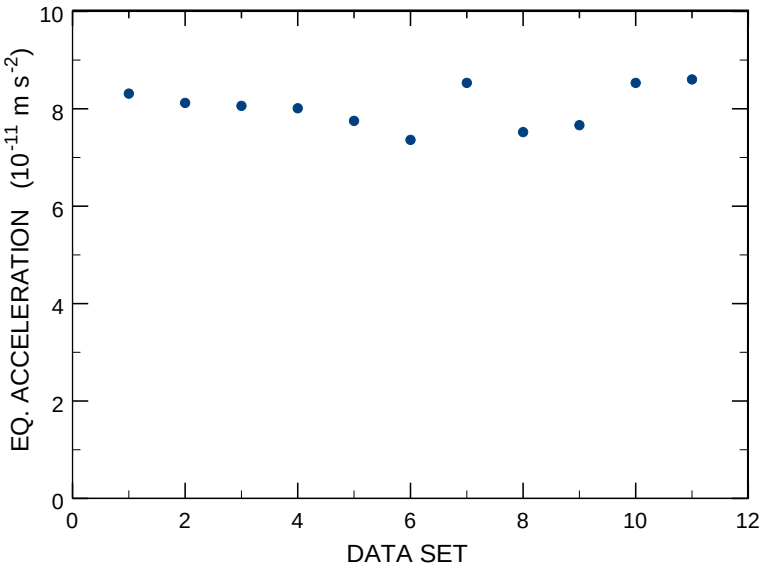

Figure B.6: Exp. III: DM $1f_s$ cross-talk.

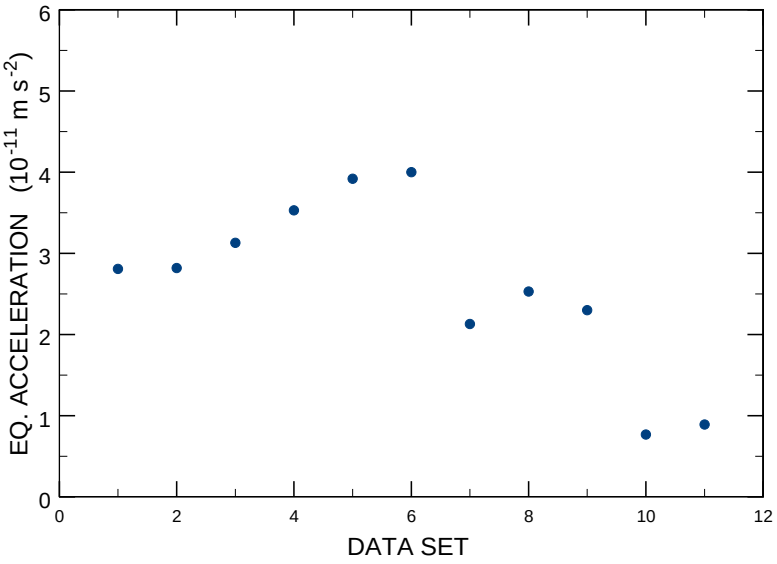

Figure B.7: Exp. III: DM $2f_s$ cross-talk.

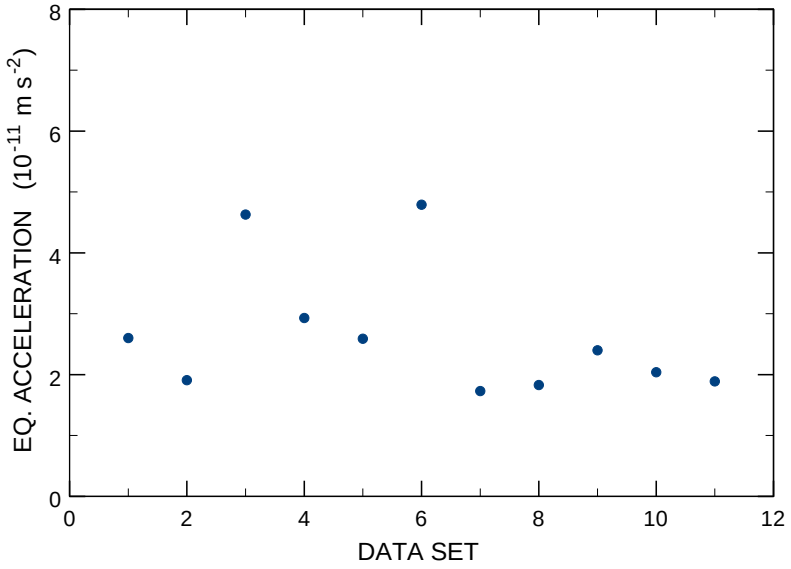

Figure B.8: Exp. III: DM $3f_s$ cross-talk.

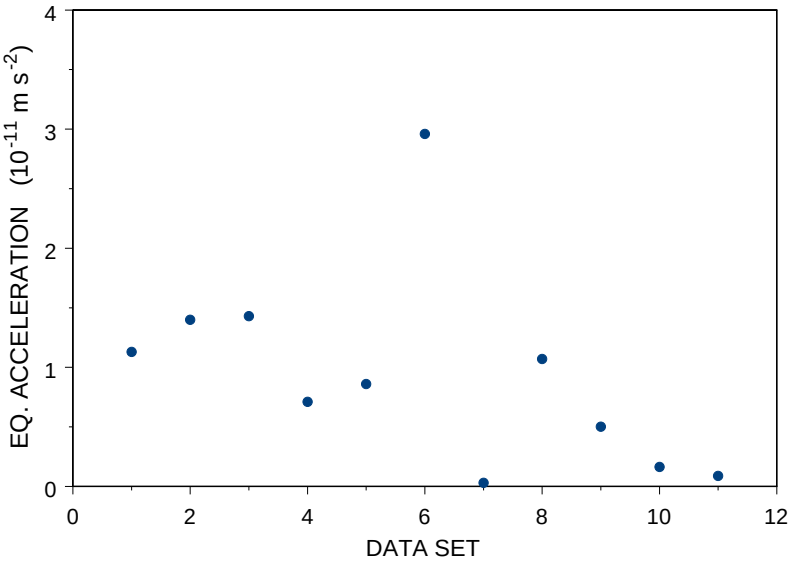

Figure B.9: Exp. III: DM $4f_s$ cross-talk.

Appendix C

Capacitance bridge

Four symmetrical plates of Nb are glued to a Macor coil form (previously used as part of the source driving coil), as shown in Fig. C.1. They are located on both sides of the source mass and the pair of plates on opposite sides are coupled and connected to form a capacitor bridge as shown in Fig. C.2. The inherent nonlinear response of a capacitor plate as a function of the gap distance can be utilized to monitor the source amplitude and position. The procedure described below worked remarkable well and provided essential data for the source position and amplitude.

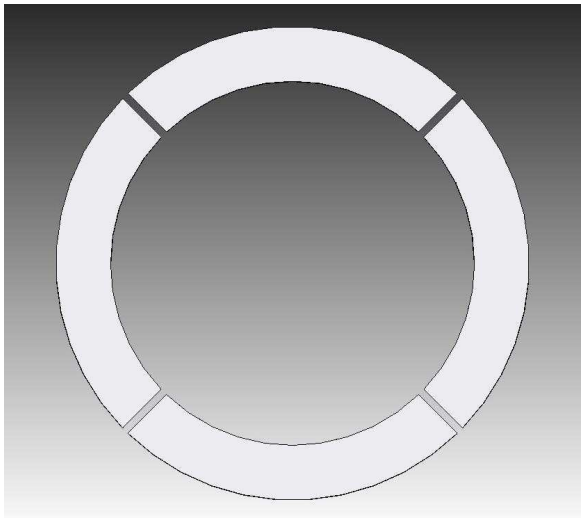

Figure C.1: Capacitor plate configuration.

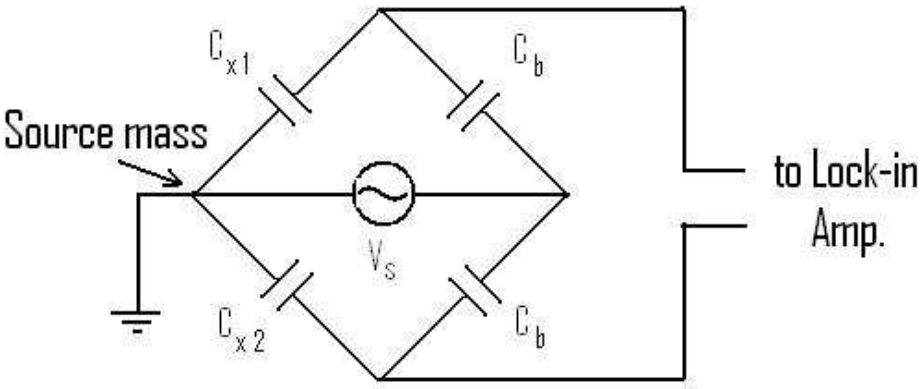

Figure C.2: Capacitor bridge circuit.

The internal oscillator of an Ithaco 3961B two-phase lock-in amplifier is used to produce a 1-mV, 1-kHz sinusoidal voltage V_S, which drives the bridge. The area of the capacitor plate is about 1.0×10^{-2} m^2. For a nominal gap of 240 μm, this corresponds to a capacitance of 90 pF. The cable leads provide an additional ~ 600 pF, thus the balance capacitors C_b are chosen to be ~ 700 pF. The output of the four bridges from the four pairs of capacitor plates were then fed to four lock-ins. Unfortunately, one of the bottom pair of capacitors was disconnected, thus we had to rely on just the other three pairs.

The output of the bridge as a function of the instantaneous source position x_s can be shown to be

$$V_o(x_s) = V_S \frac{\frac{1}{C_s+C_{x1}(x_s)}}{\frac{1}{C_s+C_{x1}(x_s)}+\frac{1}{C_b}} - \frac{\frac{1}{C_s+C_{x2}(x_s)}}{\frac{1}{C_s+C_{x2}(x_s)}+\frac{1}{C_b}}, \tag{C.1}$$

where C_s is the stray capacitance from the leads (assumed to be the same), C_b is

the balance capacitor, and

$$C_{x1}(x_s) = \frac{\epsilon_0 A_c}{x_g + x_o + x_s(t)}, \tag{C.2}$$

$$C_{x2}(x_s) = \frac{\epsilon_0 A_c}{x_g - x_o - x_s(t)}. \tag{C.3}$$

Here, x_g is the nominal sum of the gaps divided by two, or the gap size if the source were perfectly centered between the plates. It is slightly different for each pair of capacitor plates and the gaps were measured with the help of a depth gauge before cool-down. x_o is the DC offset in the source position with respect to the plates and A_c is the area of a plate. All the quantities other than x_s and x_o are directly measurable or known. Therefore, we do a fit of the capacitor plate output and Eq. (C.1) with x_s and x_o as unknowns.

The output of the bridge is recorded for a period of a 500 cycles and then signal averaged (at the source frequency) to reduce the noise from other source and detector modes. Figure C.3 shows an example, which yielded $x_S = 97$ μm and $x_0 = -9$ μm.

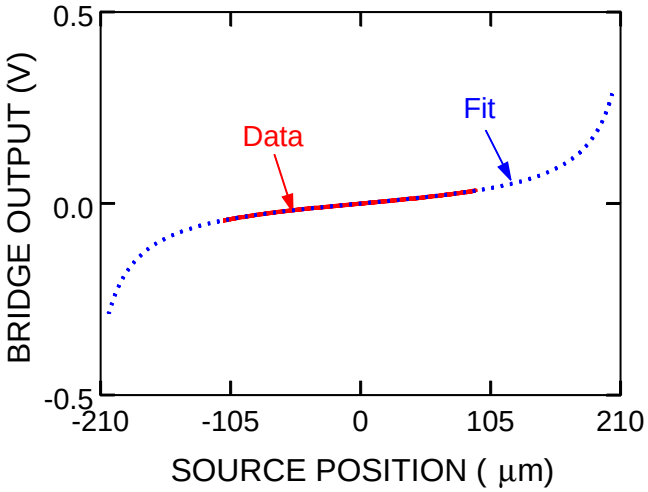

Figure C.3: Source position and amplitude determined from the capacitor bridge.

Appendix D

Weighted total least squares regression

The procedure for weighted total least squares regression was obtained from [31, 32]. To obtain the best fit line of the form $y = a + bx$, we minimize the action S, which can be expressed as

$$S = \sum_{i=1}^{N} \frac{(y_i - bx_i - a)^2}{\sigma_{yi}^2 + (b\sigma_{xi})^2}. \tag{D.1}$$

Henceforth, the sum will be assumed to be over the N points. Differentiating S with respect to a and b, we get

$$\frac{\partial S}{\partial a} = -\sum \frac{2(y_i - bx_i - a)}{\sigma_{yi}^2 + (b\sigma_{xi})^2} = 0 \tag{D.2}$$

and

$$\frac{\partial S}{\partial b} = -\sum \left\{ \frac{2(y_i - bx_i - a)(-x_i)}{\sigma_{yi}^2 + (b\sigma_{xi})^2} - \frac{(y_i - bx_i - a)^2}{[\sigma_{yi}^2 + (b\sigma_{xi})^2]^2} \sigma_{xi}^2 \right\} = 0. \tag{D.3}$$

We can solve these two equations for a and b. We use standard error propagation law to find the uncertainty in these parameters, as follows:

$$s_a^2 = \sum \left[\left(\frac{\partial a}{\partial x_i} \sigma_{xi} \right)^2 + \left(\frac{\partial a}{\partial y_i} \sigma_{yi} \right)^2 \right] \tag{D.4}$$

and

$$s_b^2 = \sum \left[\left(\frac{\partial b}{\partial x_i} \sigma_{xi} \right)^2 + \left(\frac{\partial b}{\partial y_i} \sigma_{yi} \right)^2 \right]. \tag{D.5}$$

As described in [32], these quantities are calculated as

$$\frac{\partial a}{\partial x_i} = w_i [bC + B(d_i - bF_i')]/\Delta, \tag{D.6}$$

$$\frac{\partial a}{\partial y_i} = w_i[BF_i' - C]/\Delta, \tag{D.7}$$

$$\frac{\partial b}{\partial x_i} = -w_i[bB + A(d_i - bF_i')]/\Delta, \tag{D.8}$$

$$\frac{\partial b}{\partial y_i} = w_i[B - AF_i']/\Delta, \tag{D.9}$$

where $w_i = 1/(s_{yi}^2 + bs_{xi}^2)$, $d_i = y_i - a - bx_i$, and $F_i' = x_i + 2bd_iw_iS_{xi}^2$. The quantities A, B, C and Δ are given by

$$A = -\sum w_i, \tag{D.10}$$

$$B = -\sum w_iF_i', \tag{D.11}$$

$$C = -\sum[w_iF_i'^2 - d_i^2w_i^2s_{xi}^2], \tag{D.12}$$

$$\Delta = AC - B^2. \tag{D.13}$$

Using these equations, we can compute s_a and s_b from the values of x_i, y_i, σ_{xi}, and σ_{yi}.

Bibliography

[1] Prieto, V. A. , *Submillimeter test of the gravitational inverse-square law using a superconducting accelerometer*, Ph.D. thesis, University of Maryland, College Park, Maryland (2007).

[2] Tu, L. C., Guan, S. G., Luo, J., Shao, C. G., and Liu, L. X., *Null test of Newtonian inverse-square law at submillimiter range with a dual-modulation torsion pendulum*, Phys. Rev. Lett. **98**, 201101 (2007).

[3] Kapner, D. J., *et al.*, *Test of the gravitational inverse-square law below the dark-energy scale*, Phys. Rev. Lett. **98**, 021101 (2007).

[4] Long, J. C., Chan, H. W., Churnside, A. B., Gulibs, E. A., Varney, M. C., and Price, J. C., *Upper limits to submillimiter-range forces from extra space-time dimensions*, Nature **421**, 922 (2003).

[5] Chiaverini, J., Smullin, S. J., Geraci, A. A., Weld, D. M., and Kapitulnik, A., *New experimental constraints on non-Newtonian forces below* 100 μm, Phys. Rev. Lett. **90**, 151101 (2003).

[6] Arkani-Hammed, N., Dimopoulos, S., and Dvali, G. R., *The hierarchy problem and new dimensions at a millimeter*, Phys. Lett. B **429**, 263-72 (1998).

[7] Peccei, R. D., and Quinn, H. R., *Constraints imposed by CP conservation in the presence of pseudoparticles*, Phys. Rev. Lett. **38**, 1440-1443 (1977).

[8] Randall, L. and Sundrum, R., *An alternative to compactication*, Phys. Rev. Lett. **83**, 4690-469 (1999).

[9] Weinberg, S., *A new light boson?*, Phys. Rev. Lett. **40**, 223-226 (1978).

[10] Wilczek, F., *Problem of strong P and T invariance in the presence of instantons*, Phys. Rev. Lett. **40**, 279-282 (1978).

[11] Paik, H. J. and Moody, M. V., *Short-range inverse-square law experiment in space*, proposal to NASA, (2008).

[12] Sundrum, R., *Fat gravitons, the cosmological constant and submillimeter tests*, Phys. Rev. D **69**, 044014 (2004).

[13] Paik, H. J., Prieto, V. A., and Moody, M. V., *Null test of the inverse-square law at 100-micrometer distance*, in *Gravitation and Astrophysics: on the Occasion of the 90th Year of General Relativity* (Proceedings of ICGA-7), eds. I. A. Nester, C. M. Chen and J. P. Hsu (World Scientific, Singapore), pp. 9-19 (2007).

[14] Camp, J. B., Darling, T. W., and Brown, R. E., *Effect of crystallites on surface potential variations of Au and graphite*, J. Appl. Phys. **71** 783-785 (1992).

[15] Camp, J. B., Darling, T. W., and Brown, R. E., *Macroscopic variations of surface potentials of conductors*, J. Appl. Phys. **69**, 7126-7129 (1991).

[16] Paik, H., J., *New null experiment to test the inverse-square law of gravitation*, Class. Quant. Grav. **11**, A133-A144 (1994).

[17] Prieto, V. A., private communications (2009).

[18] Chen, L., private communications (2009).

[19] Chan, H. A. and Paik, H. J., *Superconducting gravity gradiometer for sensitive gravity measurements. I. Theory*, Phys. Rev. D **35**, 3551-3571 (1987).

[20] Chan, H. A., Moody, M. V., and Paik, H. J., *Superconducting gravity gradiometer for sensitive gravity measurements. II. Experiment*, Phys. Rev. D **35**, 3572-3597 (1987).

[21] Parke, Joel W., *Null test of the gravitational inverse-square law and the development of a superconducting six-axis accelerometer*, PhD. thesis, University of Maryland, College Park, Maryland (1990).

[22] Moody, M. V., Paik, H. J., and Canavan, E., *Three-axis superconducting gravity gradiometer for sensitive gravity experiments*, Rev. Sci. Inst. **73**, 3957-3974 (2002).

[23] Robertson, N. A., Blackwood, J. R., Buchman, S., Byer, R. L., Camp, J., Gill, D., Hanson, J., Williams, S., and Zhou, P., *Kelvin probe measurements: investigations of the patch effect with applications to ST-7 and LISA*, Class. Quantum Grav. **23**, 2665-2680 (2006).

[24] Speake, C. C., *Forces and force gradients due to patch fields and contact-potential differences*, Class. Quantum Grav. **13**, A291-A297 (1996).

[25] C. C. Speake, *Interaction potential between extended bodies*, Phys. Rev. Lett. **60**, 107501 (1996).

[26] Speake, C. C. and Trenkel C., *Forces between conducting surfaces due to spatial variations of surface potential*, Phys. Rev. Lett. **90**, 160403 (2003).

[27] Antonini, P., Bimonte, G., Bressi, G., Carugno, G., Galeazzi G., Messineo, G., and Ruoso, G., *An experimental apparatus for measuring the Casimir effect at large distances*, J. Phys.: Conference Series **161**, 012006 (2009).

[28] Kim, W. J., Sushkov, A. O., Dalvit, D. A. R., and Lamoreaux, S. K., *Surface contact potential patches and Casimir force measurements*, Phys. Rev. A **81**, 022505 (2010).

[29] Casimir, H. B. G., *On the attraction between two perfectly conducting plates*, Proc. Kon. Nederland. Akad. Wetensch. **51**, 793-795 (1948).

[30] Moody, M. V., private communications (2008).

[31] Cecchi, G. C., *Error analysis of the parameters of a least-squares determined curve when both variables have uncertainties*, Meas. Sci. Technol. **2** 1127-1128 (1991).

[32] Moreno, C. and Bruzzone, H., *Parameters' variances of a least-squares determined straight line with errors in both coordinates*, Meas. Sci. Technol. **4** 635636 (1993).

[33] Taylor, J. R., *An introduction to error analysis* (University Science Books, Sausalito, 1982).

[34] Rose-Innes, A. C. and Rowland, J. J., *A simple low temperature thermal 'switch', using adsorption pump*, J. Phys. E: Sci. Instrum. **5** 939 (1972).